External photoevaporation of protoplanetary discs in Cygnus OB2: linking discs to star formation dynamical history

Andrew J. Winter ®,★ Cathie J. Clarke and Giovanni P. Rosotti ®

Institute of Astronomy, Madingley Road, Cambridge CB3 0HA, UK

ABSTRACT

Many stars form in regions of enhanced stellar density, where stellar neighbours can have a strong influence on a protoplanetary disc (PPD) population. In particular, far-ultraviolet (FUV) flux from massive stars drives thermal winds from the outer edge of PPDs, accelerating disc destruction. Here, we present a novel technique for constraining the dynamical history of a star-forming environment using PPD properties in a strongly FUV-irradiated environment. Applying recent models for FUV-induced mass-loss rates to the PPD population of Cygnus OB2, we constrain the time since primordial gas expulsion. This is 0.5 Myr ago if the Shakura & Sunyaev α-viscosity parameter is $\alpha = 10^{-2}$ (corresponding to a viscous time-scale of $\tau_{\rm visc} \approx 0.5$ Myr for a disc of scale radius 40 au around a $1\,M_\odot$ star). This value of α is effectively an upper limit, since it assumes efficient extinction of FUV photons throughout the embedded phase. This gas expulsion time-scale is consistent with a full dynamical model that fits kinematic and morphological data as well as disc fractions. We suggest Cygnus OB2 was originally composed of distinct massive clumps or filaments, each with a stellar mass $\sim 10^4\,M_\odot$. Finally we predict that in regions of efficient FUV-induced mass-loss, disc mass $M_{\rm disc}$ as a function of stellar host mass $m_{\rm star}$ follows a power law with $M_{\rm disc} \propto m_{\rm star}^{\beta}$, where β exceeds ~ 2.7 – steeper than correlations observed in regions of moderate FUV flux ($1 < \beta < 1.9$). This difference offers a promising diagnostic of the influence of external photoevaporation in a given region.

Key words: accretion, accretion discs – protoplanetary discs – circumstellar matter – stars: kinematics and dynamics – open clusters and associations: individual: Cygnus OB2 .

1 INTRODUCTION

The majority of stars form and spend their early stages of evolution in regions of enhanced stellar density (Lada & Lada 2003). This might be as part of a gravitationally bound cluster, or if star formation efficiency is sufficiently low this environment can become a short-lived association (Lada & Lada 2003; Murray 2011; Pfalzner & Kaczmarek 2013). This latter case is expected to be common (although see Kruijssen 2012), therefore understanding the effect of clustered environments on the early stages of stellar evolution is important even for apparently isolated stars.

In particular, feedback from the stellar environment has been shown to have a significant impact on planet formation in young clusters and associations. Protoplanetary disc (PPD) lifetimes are thought to be $\sim$3–10 Myr (e.g Haisch, Lada & Lada 2001;

Williams & Cieza 2011; Ribas, Bouy & Merín 2015), during which period a star typically remains in its formation environment. In this case, PPD destruction can be induced due to close star-disc encounters (Clarke & Pringle 1993; Ostriker 1994; Pfalzner et al. 2005; Breslau et al. 2014; Cuello et al. 2018; Vincke & Pfalzner 2018; Winter et al. 2018a; Concha-Ramírez, Vaher & Portegies Zwart 2019) or far-ultraviolet (FUV) driven external photoevaporation (and, to a lesser extent, extreme ultraviolet – EUV, Johnstone, Fabian & Taylor 1998; Störzer & Hollenbach 1999; Armitage 2000; Adams 2010; Facchini, Clarke & Bisbas 2016; Haworth et al. 2018a; Winter et al. 2018b). Recent studies suggest that, statistically speaking, the dominant disc dispersal mechanism is external photoevaporation (Scally & Clarke 2001; Winter et al. 2018b), while encounters can set PPD initial conditions during the evolution of stellar multiple systems (Bate 2018; Winter, Booth & Clarke 2018c).

FUV radiation has a significant influence on disc evolution in a wide range of environments. Mass-loss from the outer edge is

★ E-mail: ajwinter@ast.cam.ac.uk

driven when the thermal energy exceeds the gravitational potential (e.g. Johnstone et al. 1998). The most obvious examples of such a process are proplyds, visible for example in the Orion Nebula Cluster (O'Dell & Wen 1994), where the finite penetration of ionizing radiation into a disc's neutral wind creates an offset (cometary) ionization front. The strong neutral winds in the Orion Nebula Cluster are driven by FUV flux of $F_{FUV} \sim 3 \times 10^4\,G_0$.[1] Since then proplyds have been found for discs which experience a factor $\gtrsim 10$ lower flux (Kim et al. 2016). Even when a proplyd is not visible, a disc can exhibit significant FUV-induced mass-loss. Haworth et al. (2017) find that in the very extended disc around IM Lup, with $F_{FUV} \sim 4\,G_0$, photoevaporation drives substantial mass-loss. A large fraction of stars form in regions where FUV flux is considerably greater than this (Fatuzzo & Adams 2008; Winter et al. 2018b).

The properties of young massive stellar clusters/associations and the giant molecular clouds (GMCs) from which they form are diverse, and the link between them is not well characterized (see Longmore et al. 2014, for a review). During formation the early cluster may undergo cold collapse (Tobin et al. 2009; Kuznetsova, Hartmann & Ballesteros-Paredes 2018), or after the expulsion of gas the stellar population may become supervirial (Goodwin 2009; Pfalzner & Kaczmarek 2013), dependent on the density and velocity dispersion of the primordial GMC. This in turn influences the evolution of mass segregation (e.g. Bonnell & Davies 1998) and substructure (e.g Goodwin & Whitworth 2004) within the cluster. Because the environment of a star has an influence on the associated PPD, the dynamical history of a cluster is closely linked with the properties of a disc population.

While many authors have attempted to account for the local environment in considering PPD evolution (e.g. Scally & Clarke 2001; Cleeves et al. 2016; Guarcello et al. 2016), none have inverted this method and used observed disc populations to put constraints on the dynamical history of a star-forming environment. This work is partly motivated by this goal.

Cygnus OB2 (Cyg OB2) is a young massive OB association in the Cygnus X region, and has been used as an empirical test of feedback mechanisms on PPD evolution. It contains many massive stars up to $\sim 100\,M_\odot$ (e.g. Massey & Thompson 1991; Wright, Drew & Mohr-Smith 2015) which contribute to strong FUV radiation fields. Guarcello et al. (2016) analysed the disc fraction within Cygnus OB2 as a function of FUV flux, and found that surviving discs were less common at small projected separations from massive stars. Other authors, such as Wright et al. (2016), have made observations which indicate a complex dynamical substructure within the association. Collating this evidence, we here aim to apply *N*-body simulations and those combining viscous disc evolution and photoevaporation to replicate observations of Cyg OB2. We will reproduce the present-day stellar kinematics and a dynamical history consistent with the observed disc fraction distribution. In this way we can shed light on both the history and the likely future of the PPD population and the stellar components.

In the remainder of this work we first review the observational constraints on the properties of Cyg OB2 in Section 2. We describe our numerical method and models in Section 3. In Section 4 we compare our models with the observational data. We draw conclusions in Section 5.

---

2 PROPERTIES OF CYGNUS OB2

2.1 Stellar population

Cyg OB2 is a young association at a distance $\sim 1.33\,kpc$ from the Sun (Kiminki et al. 2015). The majority of members formed $3-5\,Myr$ ago (Wright et al. 2010), although some stars have ages as young as $\sim 2\,Myr$ (Hanson 2003) and as old as $\sim 7\,Myr$ (Drew et al. 2008). Estimates of the total stellar mass of Cyg OB2 have varied in the range 2–$10 \times 10^4\,M_\odot$ (Knödlseder 2000; Hanson 2003; Drew et al. 2008; Wright et al. 2010), although Wright et al. (2015) find a slightly lower mass of $\sim 1.6 \times 10^4\,M_\odot$ within a radius of 13 pc of the apparent centre. This includes a population of ~ 169 OB stars, the most massive of which is $\sim 100\,M_\odot$ with an age of $\sim 2\,Myr$. Cyg OB2 does not exhibit evidence of mass segregation, whereby the most massive stars occupy regions with the greatest gravitational potential (Wright et al. 2014b).

The initial mass function (IMF) at the high-mass end is not agreed upon in the literature, with many authors arriving at different conclusions (Massey & Thompson 1991; Massey, Johnson & Degioia-Eastwood 1995; Knödlseder 2000; Kiminki et al. 2007; Wright et al. 2010; Comerón & Pasquali 2012). Wright et al. (2015) take into account massive stars which have evolved to their end state. In this way they find that the observed stellar masses follow an IMF $\zeta(m) \propto m^{-2.39 \pm 0.19}$ at high masses, which is approximately consistent with the 'universal' IMF of Kroupa (2001) (or indeed a Salpeter 1955, IMF). However, inferring the high-mass IMF is problematic since the occurance of supernovae in Cyg OB2 remains a point of debate (see Butt et al. 2003 and discussion in Wright et al. 2015).

Wright et al. (2016) describe the spatial density distribution in Cyg OB2 with an Elson, Fall, and Freeman profile (EFF profile, hereafter Elson, Fall & Freeman 1987):

$$\rho = \rho_0 \left(1 + \frac{r^2}{a_{stars}^2} \right)^{-\frac{\gamma+1}{2}}, \qquad (1)$$

where $a_{stars} = 7.5\,pc$ and $\gamma = 5.8$. Normalizing for the total mass of the cluster this makes the central mass density $\rho_0 \approx 22\,M_\odot\,pc^{-3}$. However, this profile was derived for a small central region of $\sim 8\,pc \times 8\,pc$, which does not enclose the estimated core radius. Hence, when we consider the distribution of the stellar mass in our models (see Section 4.3.2) we will focus on reproducing the mass enclosed within a projected radius of 13 pc (Wright et al. 2015).

2.2 Velocity dispersion

Wright et al. (2016) presented a high-precision proper motion study of the X-ray sources in Cyg OB2. They found that the region is gravitationally unbound and exhibits an anisotropic velocity dispersion with proper motion components $\sigma_\alpha = 13.0^{+0.8}_{-0.7}\,km\,s^{-1}$ and $\sigma_\delta = 9.1^{+0.5}_{-0.5}\,km\,s^{-1}$. The radial velocity dispersion has also been measured to be $\sigma_r \sim 10\,km\,s^{-1}$, although systematic overestimates due to the binary fraction introduce uncertainties (Kiminki et al. 2007, 2008).

Interestingly Wright et al. (2016) found little evidence for expansion (or contraction) in the velocity field when considering the large-scale variations of the proper motion distribution. This finding is independent of the definition of the centre of the association, and was argued by dividing proper motions into radial and azimuthal components. The ratio of kinetic energy between the radial and azimuthal directions was found to be approximately $60:40$. In the radial (projected) velocities, no bias is found towards or away from

the centre. Azimuthally there is some preference for a ratio 66 : 34 in favour of kinetic energy in the direction of negative PA. Because Cyg OB2 is not bound, this is interpreted by Wright et al. (2016) as a remnant of the angular momentum of the primordial GMC.

2.3 Substructure

Interpretation of the internal substructure in Cyg OB2 is not straightforward. Knödlseder (2000) concluded that it is a spherically symmetric region with a diameter of ∼2° (46 pc). Since then, a number of authors have suggested a more complex morphology:

(i) Bica, Bonatto & Dutra (2003) suggested that Cyg OB2 is home to two open clusters which can be seen towards the centre. However, Guarcello et al. (2013) note that the two apparent clusters are divided by a bright nebula. This makes it unclear if the two are physically separate or merely appear so due to the higher extinction in the intervening region.

(ii) Wright et al. (2010) found evidence of populations within Cyg OB2 with distinct ages, $3.5^{+0.8}_{-1.0}$ Myr and $5.25^{+1.5}_{-1.0}$ Myr for central and north-western regions, respectively. Ostensibly, this suggests multiple star-forming events. However, the ages in physically separated regions exhibited a wide spread such that they are almost consistent with being coeval. Further the authors acknowledge a number of sources of uncertainty, including variability in pre-MS stars (Herbst et al. 1994), binarity (Preibisch & Zinnecker 1999), variable accretion (Baraffe, Chabrier & Gallardo 2009), or non-uniform extinction (Guarcello et al. 2012).

(iii) A large number of A stars were identified south of the apparent centre by Drew et al. (2008). This population appears distinct spatially and non-coeval with the OB population (although the estimated ages ∼5–7 Myr are nearly consistent with coevality within uncertainties). As the authors note, it is also possible that these stars are actually behind Cyg OB2 along the line of sight and wrongly associated due to projection (Schneider et al. 2006).

(iv) Guarcello et al. (2013) used a critical side length criterion in the mimimum spanning tree of the disc-bearing population to suggest that Cyg OB2 has a clumpy substructure. However, as stated by the authors, the definitions of these clumps are dependent on the definition of the critical side length. Additionally the non-uniform extinction due to foreground gas complicates this argument as in the case of the two open clusters identified by Bica et al. (2003).

(v) Perhaps the best evidence for underlying structure in Cyg OB2 has been the proper motion study of Wright et al. (2016). On small scales they found evidence for kinematic substructure, which is the correlation of proper motion vectors with position. Applying a Moran's I statistic (Moran 1950) they found correlation with a significance of 9.7σ and 12.5σ in RA and Dec. velocity components, respectively.

2.4 PPD population

Guarcello et al. (2016) studied the correlation between the fraction of surviving PPDs as a function of the local FUV and EUV intensity. They use a sample of 7924 X-ray sources (Wright et al. 2014a), for which the presence (absence) of a PPD is inferred by the presence (absence) of an infrared excess in the photometric data compiled from numerous surveys (see Guarcello et al. 2013). Subsequently they estimate the local flux as a function of projected separation from each O star (see Guarcello et al. 2007). The disc fractions as a function of F_{FUV} are divided into six bins between ∼10^3 and

∼5×10^4 G_0. Over this space the disc fraction drops monotonically from ∼40 per cent to 18 per cent with FUV intensity (see fig. 3 in Guarcello et al. 2016). These observations are discussed in the context of modelling in Section 4.2.

2.5 Observational summary and modelling challenges

Cyg OB2 is a well-studied young association, and as such a large number of physical characteristics serve as constraints and measures for the success of any modelling attempts. Some such metrics are as follows:

(i) Wright et al. (2016) find that the velocity dispersion in Cyg OB2 is anisotropic. This suggests that the stars share the systematic large-scale velocity field of the primordial GMC. We will find that such observations cannot be reproduced by simple models without underlying substructure, and we consider the initial properties required in Section 4.3.1.

(ii) Cyg OB2 presently has a central mass of ∼1.6×10^4 $M_\odot$ within 13 pc of the centre. Any dynamical model should match this central density after evolving for the age of the association (∼3–5 Myr). The initial stellar mass required to maintain this central density is explored in Section 4.3.2.

(iii) Although Cyg OB2 is gravitationally unbound with a large velocity dispersion, there is no bias (inwards or outwards) in the radial component of kinetic energy. This apparently suggests a lack of recent rapid expansion, despite the high velocities. When we consider our final N-body model, we will explore what expansion metric we would 'observe' (Section 4.3.4).

(iv) Statistical measures of the proper motion distribution suggest kinematic substructure which is probably indicative of stars travelling together as small virialized groups (Wright et al. 2016). We consider evidence for kinematic substructure for our final N-body model in Section 4.3.4.

(v) The disc fraction as a function of (projected) FUV field strength (Guarcello et al. 2016) provides a constraint on the length of time for which external photoevaporation has been an efficient mechanism in Cyg OB2. This allows us to put constraints on the gas expulsion time-scale. We perform these calculations to constrain the appropriate N-body model in Section 4.2, then revisit the PPD properties obtained from our final model in Section 4.4.

3 NUMERICAL METHOD

The goal of our models is to reproduce the observed dynamical properties of the stellar population and the observed fractions of surviving discs. The latter is achieved by tracking the FUV flux experienced by PPDs evolving within a given N-body model. In this section we discuss the modelling procedure applied to both the stellar dynamics (Section 3.1) and the disc evolution (Section 3.2).

3.1 Kinematic modelling

The dynamical evolution of the stellar population is calculated using NBODY6++GPU (Wang et al. 2015). This is an MPI/GPU accelerated version of NBODY6 (Spurzem 1999; Aarseth 2003), and has built-in routines to deal with the evolution of a stellar cluster within a (gas) potential. As the stellar components of Cyg OB2 are presently highly supervirial, the latter feature is necessary for an initially virialized state.

3.1.1 Gas potential

The complex nature of Cyg OB2 means that some simplifying assumptions are required for dynamical modelling. We first assume that the cluster was initially in virial equilibrium due to the contribution to the gravitational potential of the gas in the primordial association. This is achieved by invoking a Plummer potential (for numerical convenience) corresponding to a gas density profile:

$$\rho_{\mathrm{gas}} = \frac{3 M_{\mathrm{gas}}}{4\pi a_{\mathrm{gas}}} \left(1 + \frac{r^2}{a_{\mathrm{gas}}^2}\right)^{-5/2}$$

where M_{gas} is the total gas mass, r is the radial distance from the centre of the association, and a_{gas} is the scale parameter. During initial tests, we have varied a_{gas} (and the stellar scale parameter a_{stars}), and although it has a mild effect on the kinematic properties of our models, the exact value (within order unity) is not crucially important. This is particularly true in the stochastically defined initial conditions of substructured models (see Section 3.1.2 below), where kinematics are more dependent on the specific realization. Physically we expect $a_{\mathrm{gas}} \gtrsim a_{\mathrm{star}}$, and we fix $a_{\mathrm{star}} = 7\,\mathrm{pc}$ (as there is no clear evidence of past expansion) and $a_{\mathrm{gas}} = 10\,\mathrm{pc}$.

For a Plummer density profile the specific gravitational potential is:

$$\phi(r) = -\frac{G M_{\mathrm{gas}}}{a_{\mathrm{gas}}} \left(1 + \frac{r^2}{a_{\mathrm{gas}}^2}\right)^{-1/2}. \tag{2}$$

The total potential in a given cluster make up of N stars of mass m_i initially at distance r_i from the centre and r_{ij} from a star of mass m_j is

$$U_{\mathrm{tot}} = \sum_i^N m_i \left(\phi(r_i) + \sum_{j \neq i}^N \frac{G m_j}{2 r_{ij}}\right). \tag{3}$$

Then using equations (2) and (3) we require that initially

$$Q_{\mathrm{vir},0} \equiv \frac{\sum_i^N m_i v_i^2}{2 U_{\mathrm{tot}}} = 0.5,$$

where v_i is the magnitude of the initial velocity of the ith star. The total gas mass is chosen to maintain initial virial equilibrium for a cluster with a given velocity dispersion.

Our prescription of gas removal introduces an expulsion time-scale τ_{exp} over which time the potential is removed. The gas mass is reduced linearly such that $\dot{M}_{\mathrm{gas}} = M_{\mathrm{gas},0}/\tau_{\mathrm{exp}}$. We vary τ_{exp} to investigate how this affects the disc population due to extinction (see Section 4.2). We fix the time at which gas expulsion is initiated to be $\tau_{\mathrm{delay}} = 1\,\mathrm{Myr}$, consistent with the age of the most massive stars in Cyg OB2 ($\sim 2\,\mathrm{Myr}$) if the cluster age is 3 Myr (the period for which we evolve the whole system). We further define $\tau_{\mathrm{gas}} \equiv \tau_{\mathrm{delay}} + \tau_{\mathrm{exp}}$. For a discussion of the influence of gas expulsion on the dynamical state of a young cluster, see Baumgardt & Kroupa (2007).

Clearly, while computationally necessary here, a Plummer potential is not a realistic reflection of the physical conditions of the primordial gas distribution during the embedded phase. Initially, gas density distributions would be physically expected to trace the stellar density (since the stars form from the gas). Subsequently we would expect gas expulsion to occur as expanding bubbles from the most massive stars in the region (e.g. Dale & Bonnell 2011; Dale et al. 2014; Ali, Harries & Douglas 2018). In terms of the cluster evolution, we therefore expect intra-clump or -filament potential to reduce faster than inter-clump potential. The influence of a geometrically complex potential on the evolution of the stellar population is certainly of interest for accurately reproducing observed kinematics and spatial distributions. However, we assume that the Plummer potential imposed here is sufficient for reproducing the global distribution of stellar positions and velocities. This is justified since we are primarily interested in preventing the rapid escape of the high-velocity stars from the central regions of Cyg OB2. This is achieved by our spherically symmetric potential.

3.1.2 Stellar initial conditions

We define three different types of stellar initial condition, which we label uniform (UNIF), fractal (FRAC), and filamentary (FILA). A uniform cluster exhibits no underlying substructure, while fractal and filamentary clusters have enhanced local number densities, and stellar positions are correlated with velocities. While the surface density of FRAC model is 'clumpy', and individual clumps can be spatially isolated, a FILA model is defined such that the (radially binned) surface density follows an EFF profile. A filamentary model captures the morphology seen in both observations and simulations of star-forming regions (e.g. Bonnell, Clark & Bate 2008; Molinari et al. 2010; André et al. 2014), however we include both FRAC and FILA models in this work to compare their properties by the metrics of interest. We discuss the generation of each set of initial conditions below.

The simplest initial conditions are UNIF models for which stellar positions are simply drawn from an EFF profile (equation 1, Elson et al. 1987). We fix $\gamma = 5.8$, consistent with the present-day value, and fix $a_{\mathrm{stars}} = 7\,\mathrm{pc}$. The magnitude of the velocities are then chosen from a Maxwell–Boltzmann distribution

$$f(v) \propto v^2 \exp(-v^2) \tag{4}$$

with a random direction, then normalized as discussed in Section 3.1.1. We note that drawing from this distribution (particularly at the high-velocity dispersions we require – see Section 4.3.1) will produce a significant number of unbound stars. It is possible that this distribution is truncated at large velocities, and indeed star formation models suggest stars might have a smaller velocity dispersion than the primordial gas (Offner, Hansen & Krumholz 2009, see Section 4.3.3).

A FRAC model is generated using the recipe fully described by Goodwin & Whitworth (2004) which we briefly review here (see also Scally & Clarke 2002; Craig & Krumholz 2013). First we define a cube with side length 2 (in arbitrary units) centred at the origin. We then divide it up into $(2P_0)^3$ sub-cubes, where P_0 is an integer (initially chosen to be unity) which dictates the number of largest scale sub-clusters. The centre of each of these represent the potential positions for the first generation of stars, $g = 1$. All positions are offset by a vector with magnitude uniformly drawn between 0 and $2^{-(g+1)}/P_0$, and random (isotropically drawn) direction. 'Parent' positions r_g have eight possible sites for 'child' positions r_{g+1} which are placed with a probability 2^{D_0-3}, where $D_0 \leq 3$ is the fractal dimension (which we fix at 2.5). Only existing children can parent future generations. We repeat this process until the number of positions greatly exceeds the number of stars in the model, at which point the members are randomly allocated to positions. The side length of the original cube is then redefined such that the initial half-mass radius matches that of an equivalent UNIF model with parameters $a_{\mathrm{stars}} = 7\,\mathrm{pc}$, $\gamma = 5.8$.

The velocities for each generation of stars $g = 1$ is chosen in the same way as for the UNIF model. Velocities for subsequent

generations $\mathbf{v}_{g+1}$ are correlated to the velocity of the parent star $\mathbf{v}_g$:

$$\mathbf{v}_{g+1} = \mathbf{v}_g + \delta\mathbf{v}_{g+1},$$

where $\delta\mathbf{v}_g$ is a velocity with a random direction and magnitude δv_g. The latter is drawn from the modified Maxwell–Boltzmann distribution

$$f(\delta v) \propto \delta v^2 \exp\left(-2^g \delta v^2\right)$$

such that child stars have velocities correlated to their parents.

A FILA model is a hybrid between FRAC and UNIF. To construct the initial conditions we first produce a FRAC model and then force the stellar positions into an EFF profile. This is achieved by dividing the radial positions into bins, with the jth bin containing $N_{c,j}$ stars approximately at radius $r_{c,j}$, and rescaling the size of each bin ($\Delta r_{c,j}$) from inside out to produce the appropriate number density with respect to imposed EFF profile:

$$\frac{N_{c,j}}{4\pi r_{c,j}^2 \Delta r_{c,j}} = \frac{\rho(r_{c,j})}{\langle m_{\text{star}} \rangle},$$

where $\langle m_{\text{star}} \rangle$ is the average stellar mass and $\rho(r)$ is defined in equation (1).

The results of this process are filament-like structures, as shown in Fig. 1, in which FRAC and FILA models are compared. In a FRAC model the density profile has hard edges and a clump-like substructure (as in Fig. 1a), while in the FILA model stellar density drops off smoothly with radius and produces filament-like substructure (as in Fig. 1b). This is because the initial clumps from which the stellar density is composed become 'stretched' radially when we impose the EFF profile, to produce several elongated distributions of stars. Both types of model demonstrate spatial and kinematic asymmetry with respect to the gas potential.

We draw stellar masses from a Kroupa (2001) IMF:

$$\xi(m) \propto \begin{cases} m^{-1.3} & \text{for } 0.08\,\text{M}_\odot \le m < 0.5\,\text{M}_\odot \\ m^{-2.3} & \text{for } 0.5\,\text{M}_\odot \le m < 1.0\,\text{M}_\odot \\ m^{-2.4} & \text{for } 1.0\,\text{M}_\odot \le m < 100\,\text{M}_\odot \\ 0 & \text{else} \end{cases}, \tag{5}$$

where at high-mass end $> 1\,\text{M}_\odot$ we use the observed mass function in Cyg OB2 (Wright et al. 2015). In our models stars are not primordially mass segregated.

Reproducing observations requires estimating an appropriate field of view, which is in turn dependent on the definition of the cluster centre. Observationally some discrepancy exists in this definition between different works, although authors generally agree within a few pc (see Wright et al. 2016, for a discussion). For our purposes an approximate estimate of this centre is sufficient as we find that all of the metrics that we consider are only weakly dependent on our choice. For UNIF models, the cluster centre remains the centre of mass of the original set-up. For FILA and FRAC models, where considerable anistropy exists in the stellar kinematic distribution, it is necessary to estimate the centre of mass for each snapshot in time. We choose an efficient (approximate) algorithm, in which we find the point which maximizes the mass within a given projected radius (chosen to be $R_{\text{cent}} = 10\,\text{pc}$) by sampling recursively over a grid of points. Providing the grid is sufficiently highly resolved, the centre we obtain is insensitive to the exact value of R_{cent} and number of iterations. All subsequent results should be understood in this context.

3.2 Disc evolution model

In this section we discuss the prescription we apply to calculate PPD evolution. Each disc is exposed to an FUV flux resulting from tracking the contributions from the stellar components within a given N-body model.

3.2.1 FUV flux and mass-loss rate

Flux in the FUV energy range ($6\,\text{eV} < h\nu < 13.6\,\text{eV}^2$) is the most efficient contributer to external photoevaporation of PPDs in an intermediate regime of distances from massive stars. As discussed by Winter et al. (2018b), extreme ultraviolet radiation can also contribute to the thermal wind, however it only dominates the mass-loss rate in regions where FUV flux is low ($F_{\text{FUV}} \lesssim 50\,\text{G}_0$) or very high ($F_{\text{FUV}} \gtrsim 10^5\,\text{G}_0$). Both of these thresholds lie outside the region of interest in Cyg OB2. Additionally, in these cases disc destruction time-scales are extremely long and short, respectively, and the additional mass-loss contributed by EUV flux in young massive clusters is therefore not significant to our consideration of the survival rates of discs on a time-scale of Myr.

To calculate the FUV luminosity for a star of a given stellar mass we apply the precription discussed by Armitage (2000) and Winter et al. (2018b). Model grids by Schaller et al. (1992) contain the total luminosities and effective temperatures of stars of a given mass, for which we use the results for metallicity $Z = 0.02$ and the output age closest to 1 Myr. We then obtain the wavelength-dependent luminosity from the atmosphere models of Castelli & Kurucz (2004). In this way we obtain an FUV luminosity for all stars with a mass m in the range $1\,\text{M}_\odot < m < 100\,\text{M}_\odot$.

For the FUV-induced mass-loss rates $\dot{M}_{\text{wind}}$ we use the recent grid of models calculated by Haworth et al. (2018b). The grid covers a wide range of parameter space in outer disc radius (1–400 au), disc masses ($\sim 10^{-8}$–$0.1\,\text{M}_\odot$), FUV field strengths (10–$10^4\,\text{G}_0$), and stellar masses (0.05–$1.9\,\text{M}_\odot$). These mass-loss rates are interpolated linearly and applied to a viscously evolving disc to establish the expected disc properties in a given cluster environment.

3.2.2 Viscous disc evolution

To calculate the state of PPDs evolving within the cluster we must take into account viscous expansion as well as the photoevaporative mass-loss. The viscous disc evolution is modelled using the method of Clarke (2007, and subsequently Anderson, Adams & Calvet 2013, Rosotti et al. 2017, and Winter et al. 2018b). In such a parametrization, viscosity is assumed to scale linearly with radius r within the disc, corresponding to a constant α-viscosity parameter (Shakura & Sunyaev 1973) and a temperature which scales with $r^{-1/2}$. The accretion rate at the inner edge of the disc is initially

$$\dot{M}_{\text{acc,0}} = \frac{3\alpha\, M_{\text{disc,0}} H_1^2 \Omega_1}{2 R_1^2}, \tag{6}$$

where $M_{\text{disc,0}}$ is the initial disc mass, H_1 and Ω_1 are the scale height and Keplerian frequency at the disc scale radius R_1 (see Hartmann et al. 1998). Providing that the outer radius of the disc $R_{\text{disc,0}}$ is significantly greater than R_1, the initial surface density can be written

$$\Sigma_0(r < R_{\text{disc,0}}) \approx \frac{M_{\text{disc,0}}}{2\pi R_1^2} \left(\frac{r}{R_1}\right)^{-1} e^{-r/R_1} \tag{7}$$

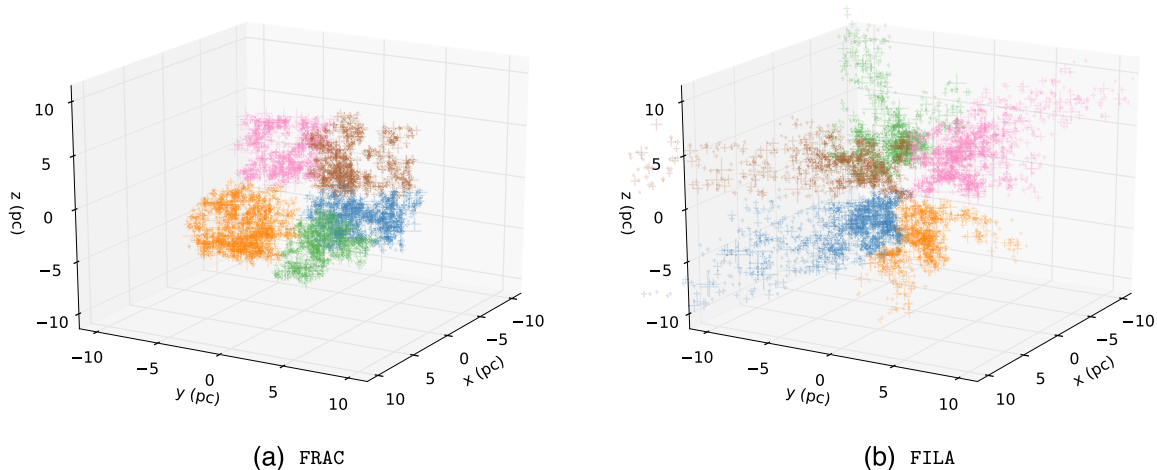[2]Photons with $h\nu > 13.6\,\text{eV}$ are considered extreme ultraviolet (EUV).

Figure 1. Example of initial position distribution of stars in `FRAC` and `FILA` models (Figs 1a and b, respectively). In the `FRAC` model, stellar positions are distributed with a 'clumpy' morphology, whereas the `FILA` model exhibits extended filaments. A subset of 5000 stars within a cube of side length 10 pc are shown, where the coordinate system is defined by the gas potential (see the text for details). Both models have a stellar mass of $10^4 \, M_\odot$ and the same half mass as an EFF profile with $a_{\text{stars}} = 7 \, \text{pc}$, $\gamma = 5.8$; the `FILA` model also follows the same radial density profile (equation 1 with the aforementioned parameters). The scatter points are coloured by the largest scale subgroup with which they are associated and scaled linearly by the mass of the star.

and $\Sigma_0(r > R_{\text{disc}, 0}) = 0$. We choose $R_{\text{disc}, 0} = 2.5 R_1$, such that the integral of equation (7) over the disc area yields 92 per cent of $M_{\text{disc}, 0}$. We take the scale radius to be

$$R_1 = 40 \left(\frac{m_{\text{star}}}{1 \, M_\odot} \right)^{1/2} \text{au}. \qquad (8)$$

Unless otherwise stated we will assume that $M_{\text{disc}, 0}$ is uniformly distributed between 0.01 and $0.1 \, m_{\text{star}}$ (Andrews et al. 2013); then equation (8) means that the distribution of initial surface densities at R_1 remains independent of stellar host mass. The scale height H is proportional to the radius throughout the disc, and we choose $H_1/R_1 = 0.05$. The maximum initial accretion rate (equation 6) as a function of stellar mass is indicated in Fig. 2. The associated viscous time-scale is

$$\tau_{\text{visc}} \approx \frac{5.4 \cdot 10^3}{\alpha} \left(\frac{R_1}{40 \, \text{au}} \right)^{3/2} \left(\frac{m_{\text{star}}}{1 \, M_\odot} \right)^{-1/2} \text{yr} \qquad (9)$$

or $\tau_{\text{visc}} \approx 0.5 \, \text{Myr}$ for a solar mass star with $\alpha = 10^{-2}$, $R_1 = 40 \, \text{au}$. Equations (8) and (9) yield $\tau_{\text{visc}} \propto m_{\text{star}}^{1/4}$.

During the course of this work we will explore the effect of altering disc initial conditions on their final properties, however we always consider a distribution of initial disc masses. Allowing a range of initial disc masses accounts for the observed range of stellar ages (since internal processes deplete the disc over time) and variable disc initial conditions. Additionally, for a given FUV flux environment some fraction of discs survive, and the findings of Guarcello et al. (2016) indicate that this survival fraction reduces monotonically with increasing F_{FUV}. We find that, depending on initial disc properties, dynamical mixing between regions of different FUV flux and the range of F_{FUV} within a single bin alone are insufficient to produce the observed survival fractions (i.e. observed survival fractions between F_{FUV} bins do not jump rapidly from ~0 per cent to ~100 per cent at a certain threshold). The chosen initial conditions and the variation between discs are therefore important in reproducing observations. Whether or not this dispersion is inherited from a tight correlation between stellar mass and PPD initial conditions
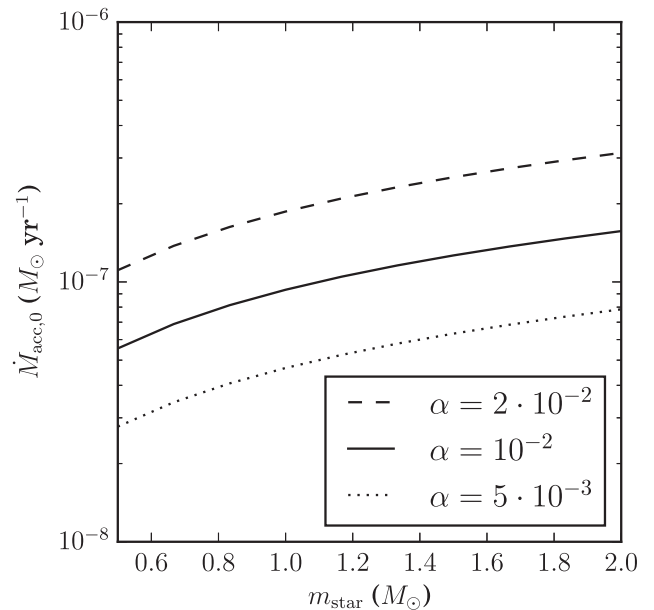

Figure 2. Assumed initial viscous accretion rate (equation 6) as a function of stellar mass for $M_{\text{disc},0} = 0.1 \, m_{\text{star}}$ and a range of Shakura & Sunyaev α-viscosity parameters. The initial disc conditions are described in Section 3.2.2. The range of stellar masses we consider (0.5–$2 \, M_\odot$) is discussed in Section 4.2.

is explored by considering host mass independent disc models in Section 4.4.3.

Using the initial conditions described above we calculate the evolution of the disc over a one-dimensional grid, spaced evenly in $r^{1/2}$. The cell at the inner edge has a zero torque boundary condition, and the cell at the outer edge experiences mass depletion due to the photoevaporation-induced wind (i.e. for a given mass-loss rate $\dot{M}_{\text{wind}}$, the disc material is removed from the outer edge).

The edge cell is then redefined depending on whether there is net mass-loss or mass accumulation (see section 4.2 in Winter et al. 2018b).

4 RESULTS AND DISCUSSION

4.1 Modelling approach

We aim to produce an *N*-body model, including initial gas potential, with a self-consistent treatment for the photoevaporation of the PPD population. We simplify the modelling procedure by the following approach:

(i) First we estimate the gas expulsion time-scale $\tau_{gas} \equiv \tau_{delay} + \tau_{exp}$ by considering the observed surviving disc fractions as a function of FUV field strength (Section 4.2). The presence of primordial gas influences the models in two ways: it imposes a gravitational potential on the stellar population, and suppresses photoevaporation by extincting FUV photons. Using the latter effect we can calibrate the period of efficient exposure to the observed survival rate of PPDs. There exists a degeneracy in this calculation with the assumed disc viscosity, and we explore the influence of varying both parameters (see Section 4.2).

(ii) Having established the rate of gas expulsion, we apply the appropriate time-dependent potential to establish the dynamical evolution of the stellar population consistent with kinematic and spatial data. In Section 4.3.1 we deduce the initial conditions required to reproduce the observed anistropic velocity dispersion. In Section 4.3.2 we vary the initial stellar mass required to reproduce the observed central density (within 13 pc of the apparent centre).

(iii) Finally we combine our findings into a 'best-fitting' model, and explore the evolution of PPDs over time in Section 4.4. This allows us both to test whether external photoevaporation is a viable mechanism for disc depletion in Cyg OB2 and to make predictions regarding the disc properties for future observations.

4.2 Disc fractions and gas expulsion

We first estimate the influence of the time-scale for gas expulsion on the PPD population survival fractions. A number of physical effects must be taken into account when considering the statistical distribution of disc fractions. Most obviously, projection effects can lead to a distribution of physical distances between stars for every apparent (projected) separation, and therefore a range of F_{FUV}. Binarity and the initial PPD properties will also influence the total disc fraction. However, to first order, the steepness of the drop-off of the disc fraction with F_{FUV} indicates the length of time for which external photoevaporation has been an efficient mechanism for disc destruction in a given enivironment. Initial tests suggest that a massive gas mass ($\gtrsim 10^6 \, M_\odot$) is required to maintain virial equilibrium in the primordial Cyg OB2. This gas mass is sufficient to dramatically reduce photoevaporation efficiency due to extinction of FUV photons.

The current PPD population therefore allows us to constrain when the gas component of Cyg OB2 was expelled. The relatively short period of expulsion ($\lesssim 2 \, Myr$) means that we are free to consider the influence of FUV photons on disc evolution from the time τ_{gas} at which gas is completely removed. Practically this means that we can apply a simplified UNIF model with the present-day mass and 'switch on' photoevaporation at different times. We then compare the disc fractions as a function of FUV flux after 3 Myr

of evolution, and thus estimate the gas expulsion time-scale. The FUV flux in those bins is calculated in the same way as in Guarcello et al. (2016), using the projected distance between stars – this we call 'projected' F_{FUV} (as opposed to 'real' F_{FUV}, as experienced by a given disc). As an estimate of the influence of dynamical mixing between projected FUV flux bins, we start with a stellar velocity dispersion 17 km s^{-1} and hold the stars in virial equilibrium with an external potential.

The rate at which irradiated discs are destroyed is also dependent on the α-viscosity parameter (Section 3.2.2). The chosen α dictates the rate at which a disc viscously expands into a region where photoevaporation rates are high, as well as dictating mass-loss through accretion. This adds a degeneracy to our approach which, given uncertainties in α, introduces similar uncertainties in τ_{gas}. We investigate this degeneracy by calculating surviving PPD fractions for a number of different values for τ_{gas} (1, 2, 2.5, and 2.75 Myr) and α (5×10^{-3}, 10^{-2}, 2×10^{-2}).

We calculate disc evolution for a subset of discs with host stars in the mass range 0.5–2 $M_\odot$. Stars less massive than this are not present in the sample used by Guarcello et al. (2016), while the disc mass-loss rates calculated by Haworth et al. (2018b) do not apply for higher mass stars. A disc is considered destroyed if it has a mass $< 10^{-5} \, M_\odot$, which is estimated by Guarcello et al. (2013) as a limit below which SEDs are more difficult to interpret. In fact discs of such low mass ($\sim 10^{-5} \, M_\odot$) are destroyed quickly in regions of strong FUV fields, so our results are insensitive to the exact value of this threshold.

The results of this preliminary modelling procedure compared with the observational findings of Guarcello et al. (2016) are summarized in Fig. 3. We expect disc fractions at lower F_{FUV} are overestimated as we do not consider other disc dispersal processes (such as internal photoevaporation, see Section 4.4). We therefore focus on matching disc fractions in regions of higher F_{FUV}. We find that $\tau_{gas} = 2.5 \, Myr$ and $\alpha = 10^{-2}$ give a good fit to the data for projected $F_{FUV} \gtrsim 3000 \, G_0$. Since we have assumed 100 per cent extinction of FUV photons before gas is completely expelled, this α is an upper limit. As discussed above, reducing the expulsion time-scale to $\tau_{gas} = 1 \, Myr$ while decreasing the viscosity such that $\alpha = 5 \times 10^{-3}$ also yields the correct disc fractions. However, if gas ejection was initiated at the time of formation of the most massive stars ($\sim 2 \, Myr$) this would suggest instantaneous expulsion, which is not physical. In this case early supernovae may be responsible for driving gas mass-loss (see discussion in Section 2.1). However, for short τ_{gas} Cyg OB2 must have had an extremely large initial stellar mass to maintain the present-day central density ($\gg 10^5 \, M_\odot$, see Section 4.3.2 and Fig. 7), which is neither supported by observations nor computationally practicable for the range of models we wish to explore.

While the simplified model presented in this section is not an accurate representation of the dynamical conditions in the region, it represents a first-order approximation on which we can base our choice of kinematic parameters in Section 4.3. We will again consider the disc fractions for a more realistic model in Section 4.4.

4.3 Stellar population properties

In this section we consider the initial conditions for our *N*-body models of the stellar population of Cyg OB2. We proceed by first aiming to reproduce the observed velocity dispersion in the region by varying the initial velocity distribution and substructure
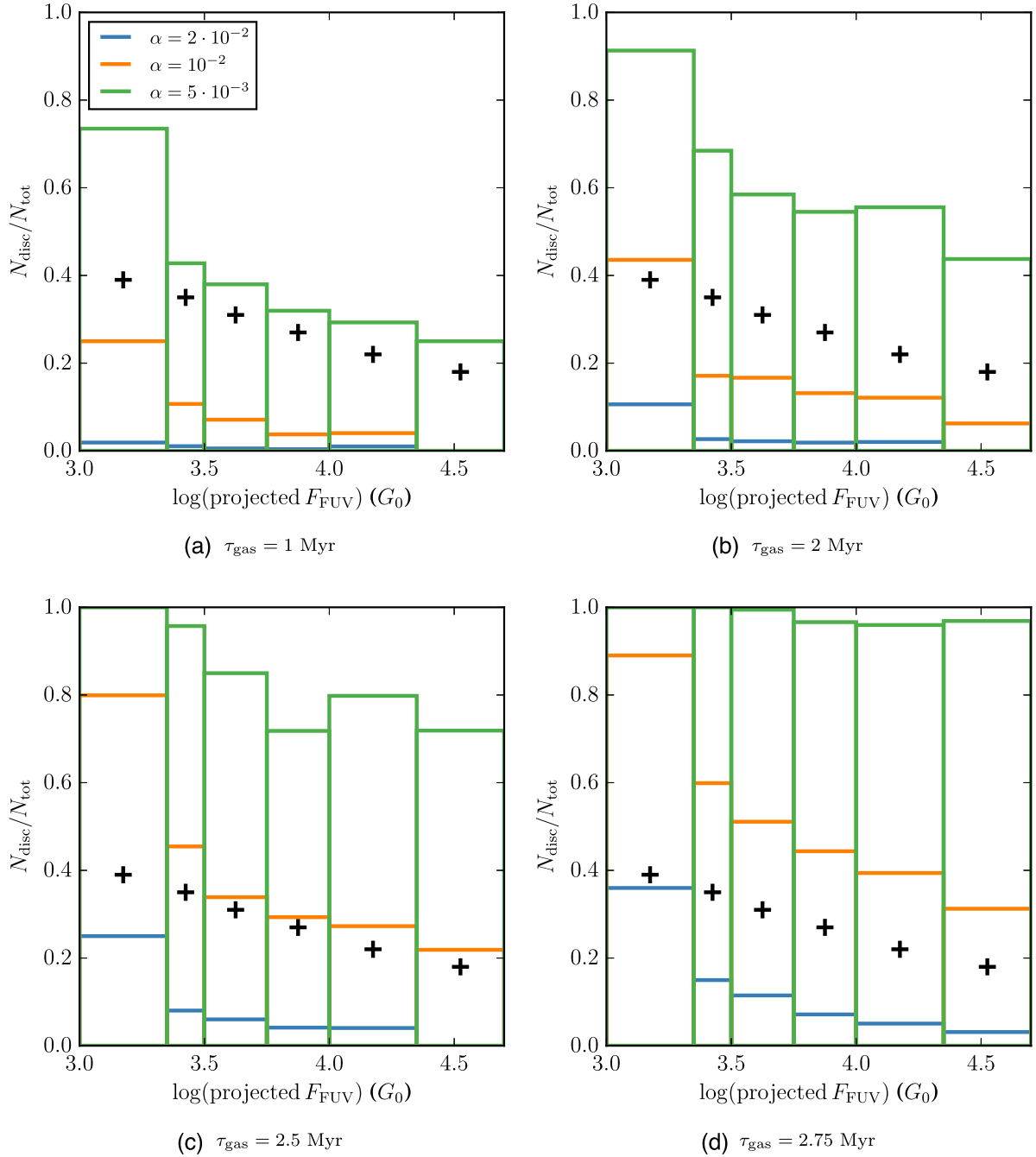
Figure 3. Disc fractions versus projected FUV flux in a virialized cluster evolved for 3 Myr when external photevaporation is 'switched on' after a period $\tau_{\rm gas}$. Results are shown for a range of Shakura & Sunyaev α-viscosity values. The black crosses represent the observational values found by Guarcello et al. (2016). These results are used to calibrate the time-scale for gas expulsion and the corresponding disc viscosity required to reproduce the observed disc fractions. We find that $\tau_{\rm gas} = 2.5$ Myr with $\alpha = 10^{-2}$ matches observed disc fraction. This value for α is effectively an upper limit since we assume that extinction efficiently shuts off photoevaporation before all gas is expelled.

(Section 4.3.1). Subsequently we match the observed central density by varying the initial stellar mass (Section 4.3.2).

4.3.1 Velocity dispersion, anisotropy, and substructure

In terms of the stellar population, the first observable quantity we aim to reproduce is the central velocity dispersion and its anisotropy

$(\langle v^2 \rangle^{1/2} \approx 17 \, {\rm km \, s^{-1}}$, and the proper motion dispersions $\sigma_{\alpha, \delta} \gtrsim \sigma_r$ the line-of-sight component – see Wright et al. 2016). This is because it is not strongly sensitive to the initial stellar mass of the cluster. We demonstrate this by considering UNIF cluster models (where cluster conditions are relatively non-stochastic) for a range of initial three-dimensional velocity dispersions and stellar masses; we plot the resuts in Fig. 4. As the potential is dominated by the gas in the cluster, and the stellar component is itself highly supervirial,
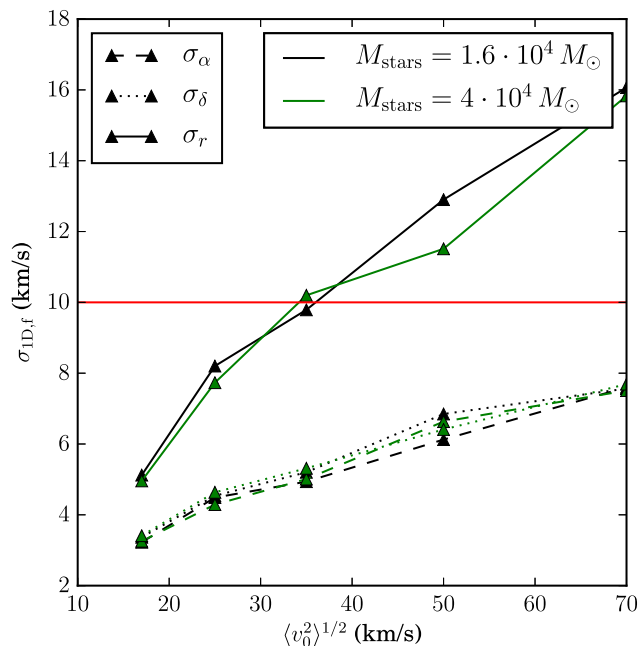
Figure 4. The components of the velocity dispersion (σ_α, σ_δ, and σ_r, where σ_r is the line-of-sight component) in our model using the Wright et al. (2016) field of view after 3 Myr of evolution versus the initial three-dimensional velocity dispersion over the entire cluster, $\langle v_0^2 \rangle^{1/2}$. The initial conditions are non-substructured (UNIF) and have initial parameters $a_{\mathrm{gas}} = 10\,\mathrm{pc}$, $a_{\mathrm{stars}} = 7\,\mathrm{pc}$, $\tau_{\mathrm{exp}} = 1.5\,\mathrm{Myr}$ and two different stellar masses $M_{\mathrm{stars}} = 1.6 \times 10^4\,\mathrm{M_\odot}$, $4 \times 10^4\,\mathrm{M_\odot}$ (black and green lines, respectively). The horizontal red line represents the mean observed one-dimensional velocity dispersion $\langle v^2 \rangle^{1/2}/\sqrt{3} \approx 10\,\mathrm{km\ s^{-1}}$. The radial (line of sight) velocity dispersion $\sigma_r > \sigma_{\alpha, \delta}$ due to projection effects and velocity sorting. Observationally we require a model such that the one-dimensional velocity dispersion components are of the same order (in fact observations indicate $\sigma_{\alpha, \delta} \gtrsim \sigma_r$). This is not reproduced by the UNIF model.

Figure 5. The components of the velocity dispersion ($\sigma_{\alpha, \delta, r}$) as in Fig. 4 but for a fixed stellar mass $M_{\mathrm{stars}} = 1.6 \times 10^4\,\mathrm{M_\odot}$. Instead of the UNIF model in Fig. 4, the black lines represent the case for a FILA cluster model and the green lines are for a FRAC cluster model, both with $P_0 = 1$ and $D_0 = 2.5$. In this case the large-scale substructure gives rise to much greater stochastic variations in the relative one-dimensional velocity dispersions, and is consistent with observations.

the final central velocity dispersion is insensitive the total stellar mass.

Fig. 4 demonstrates that UNIF models fail to reproduce the observed velocity dispersion. This is because in a non-substructured model we find supressed proper motion velocity dispersions $\sigma_{\alpha, \delta}$ with respect to the radial component σ_r, since stars with high velocities in the plane of the sky preferentially leave the central field of view over time (velocity sorting). To remedy this, we need to incorporate substructure into our model.

To demonstrate the influence of substructure on the components of the velocity dispersion within a finite field of view, we run FILA and FRAC models with large-scale substructure ($P_0 = 1$), and rotate a snapshot at 3 Myr such that the radial velocity dispersion is approximately minimized. The results of this process are shown in Fig. 5, where the decomposed velocity components are again compared with the initial three-dimensional velocity dispersion. The anisotropies in the velocity dispersion are reproduced in both FILA and FRAC cluster models.

The degree of anisotropy in the velocity dispersion is dependent on the scale of substructure. Fig. 6 shows the results for initially smaller filaments/clumps (using $P_0 = 2$). While there still exist stochastic fluctuations in the components of the velocity dispersion, the degree of anisotropy is not sufficient to yield proper motion velocity dispersions greater than the radial component. This suggests
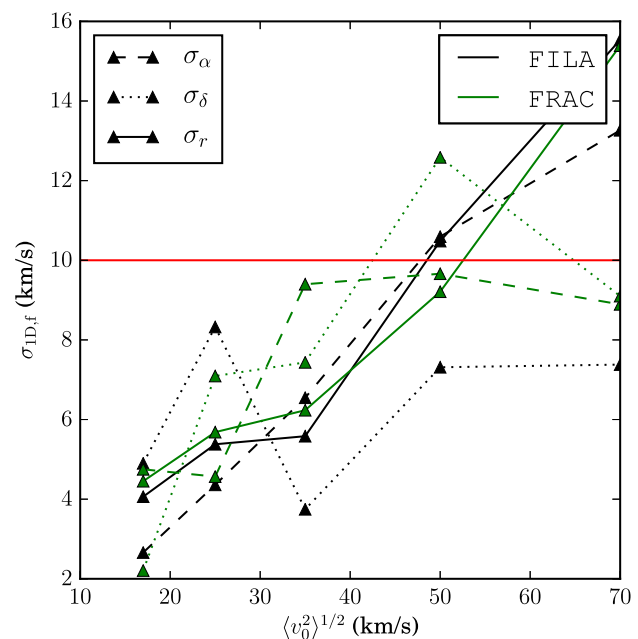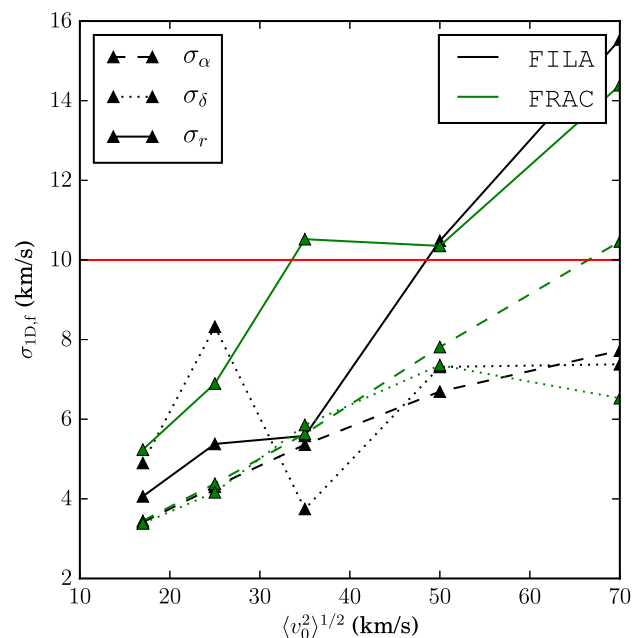

Figure 6. The same as in Fig. 5 but with smaller scale substructure ($P_0 = 2$). In this case the scale of substructure is insufficient to result in proper motion velocity dispersions comparable to the radial dispersion (we have $\sigma_{\alpha, \delta} < \sigma_r$).

that the initial region consisted of large clumps or filaments of mass $\sim 10^4 \, M_\odot$.

We estimate that the required initial velocity dispersion in Cyg OB2 is $\langle v_0^2 \rangle^{1/2} \sim 50 \, \text{km s}^{-1}$, although the stochasticity of the substructured models makes precise estimates impractical. In future models we will assume this is the initial three-dimensional velocity dispersion. Other required parameters, such as the initial stellar mass, are chosen to be consistent with this property.

4.3.2 Central mass

We wish to alter the initial stellar mass such that the central density at the end of the simulation is consistent with observations. A cluster model with a central mass of $1.6 \times 10^4 \, M_\odot$ after 3 Myr of evolution is required, where $\langle v_0^2 \rangle^{1/2} = 50 \, \text{km s}^{-1}$ as discussed in Section 4.3.1. To find the appropriate initial mass we run UNIF, FRAC, and FILA models at stellar masses $M_{\text{stars}} = 2 \times 10^4 \, M_\odot$, $4 \times 10^4 \, M_\odot$, and $8 \times 10^4 \, M_\odot$. The results are shown in Fig. 7. We find that $M_{\text{stars}} = 8 \times 10^4 \, M_\odot$ (Fig. 7c) is sufficient to yield the required central mass after 3 Myr of evolution.

Neither the initial mass nor the substructure has a significant effect on the fraction of the stellar mass which remains within a 13 pc projected radius (approximately a quarter in each case). As in the case of our velocity investigation, this is due to the fact that the stellar component of the potential energy is much smaller than the total kinetic energy.

The central mass in all of our models undergoes a similar temporal evolution. In Fig. 7 we see an initial rapid mass-loss as stars with the highest energies escape the potential. This is because we do not truncate the velocity dispersion such that escapers are initially forbidden; it is not clear whether or not this is physically realistic, and the effect of choosing such initial conditions is discussed in Section 4.3.3 in the context of primordial gas mass. However, since stars which escape the central regions are not considered in our PPD models and the gravitational potential is dominated by the gas component, whether or not these early escapers are initially included in the model is of secondary importance. After this initial decline in mass, some high-energy stars remain bound, and therefore return to the central regions, causing a modest oscillation in the mass. This is again a consequence of using a Boltzmann velocity distribution without truncating the high-velocity end. The magnitude of this oscillation is more variable for substructured regions where velocities (and therefore kinetic energies) are correlated. Gas expulsion (starting at $\tau_{\text{delay}} = 1 \, \text{Myr}$ and continuing over $\tau_{\text{exp}} = 1.5 \, \text{Myr}$) results in a decrease in gravitational potential, and as the number of stars with energies sufficient to escape increases, the central mass decreases.

4.3.3 Summary of best-fitting model

By considering gas expulsion, stellar mass, velocity dispersion, and initial substructure, we have found a model for the evolution of Cyg OB2, summarized by the parameters in Table 1, which fits observations of the stellar population. While we refer to this as our 'best-fitting' model, this is to be understood as the result of our process of deduction in terms of the appropriate parameters, and not as the optimization of a statistical metric or parameter space exploration. In our models we find gas expulsion was completed $\sim 0.5 \, \text{Myr}$ ago (for a PPD viscous time-scale of 0.5 Myr), the initial velocity dispersion was $\sim 50 \, \text{km s}^{-1}$ and the initial cluster mass was $\sim 8 \times 10^4 \, M_\odot$. We further suggest that the largest scales of

initial coherent clumps within the primordial Cyg OB2 had a mass of $\sim 10^4 \, M_\odot$. No significant dynamical differences can be found between FRAC and FILA type models at the present time, and we hereafter use a FILA model in our analysis of the disc population (Section 4.4).

The gas mass required for initial virial equilibrium is $M_{\text{gas}} \sim 8 \times 10^6 \, M_\odot$ (with a scale parameter $a_{\text{gas}} = 10 \, \text{pc}$). This would make the primordial GMC massive compared to known Milky Way molecular clouds, although the census is not complete (see Longmore et al. 2014, for a review). It is also possible that the initial velocity dispersion is overestimated due to the truncation of equation (4) at high velocities (simulations suggest stars have a subvirial initial velocity dispersion with respect to the primordial gas – see Offner et al. 2009; Kruijssen 2012). While this would not influence the central velocity dispersion (high-velocity stars leave the centre in any case) it would reduce the number of escapers early on in the cluster evolution and therefore the required initial stellar mass. It would also reduce the gas mass necessary for virial equilibrium as $M_{\text{gas}} \propto \langle v^2 \rangle$ if $M_{\text{gas}} \gg M_{\text{stars}}$ (equation 3). If our gas mass estimate is accurate then this makes the star formation efficiency ~ 1 per cent, although this is probably a lower limit (an upper limit on M_{gas}).

4.3.4 Substructure and expansion observables

Alternate kinematic constraints not considered in the previous analysis include the measures of substructure and the absence of expansion signatures in the stellar kinematics (Wright et al. 2016). We find that determining these metrics is problematic for a given cluster model. This is because the values obtained differ stochastically depending on initial conditions, the time of 'observation' and the subset of stars used in taking a measurement. To obtain an accurate probability of finding the observed values for these metrics, a large number of models would need to be tested, which would be computationally expensive. However, for our chosen model the velocity field is illustrated in Fig. 8. We find that the correlation between positions and proper motions is clear (Fig. 8a), while Fig. 8(b) does not show clear evidence of expansion. However, the stellar components are in fact expanding globally since they are unbound.

To illustrate this point more fully, we define the expansion parameter:

$$\mathcal{E} = \frac{T^+}{T^- + T^+}, \tag{10}$$

where $T^{+/-}$ is defined as the total kinetic energy of stars directed in the postive/negative projected radial direction (in the plane of the sky). Thus $\mathcal{E} \rightarrow 1$ or 0 if the velocity dispersion indicates rapid expansion or contraction, respectively. A value of $\mathcal{E} \approx 0.5$ would usually be taken as evidence that a stellar population is not expanding. In Fig. 9 we show the cumulative distribution of the measured expansion parameter for random subsets of 800 stars in the Wright et al. (2016) field of view (the central 8 pc × 8 pc). We find that a wide range of values for $\mathcal{E}$ is possible at any given time. Depending on the time at which the velocities are observed and the chosen subsample, our model is found to be consistent with an observed value $\mathcal{E} \approx 0.5$. This is because the $\mathcal{E}$ distribution varies considerably and non-monotonically in time even for a single model. However, at any given time the stellar population is expanding (filaments are moving away from each other). Alternative geometrical signatures may be more successful at gauging such expansion. Due to the stochasticity and wide range of possible $\mathcal{E}$
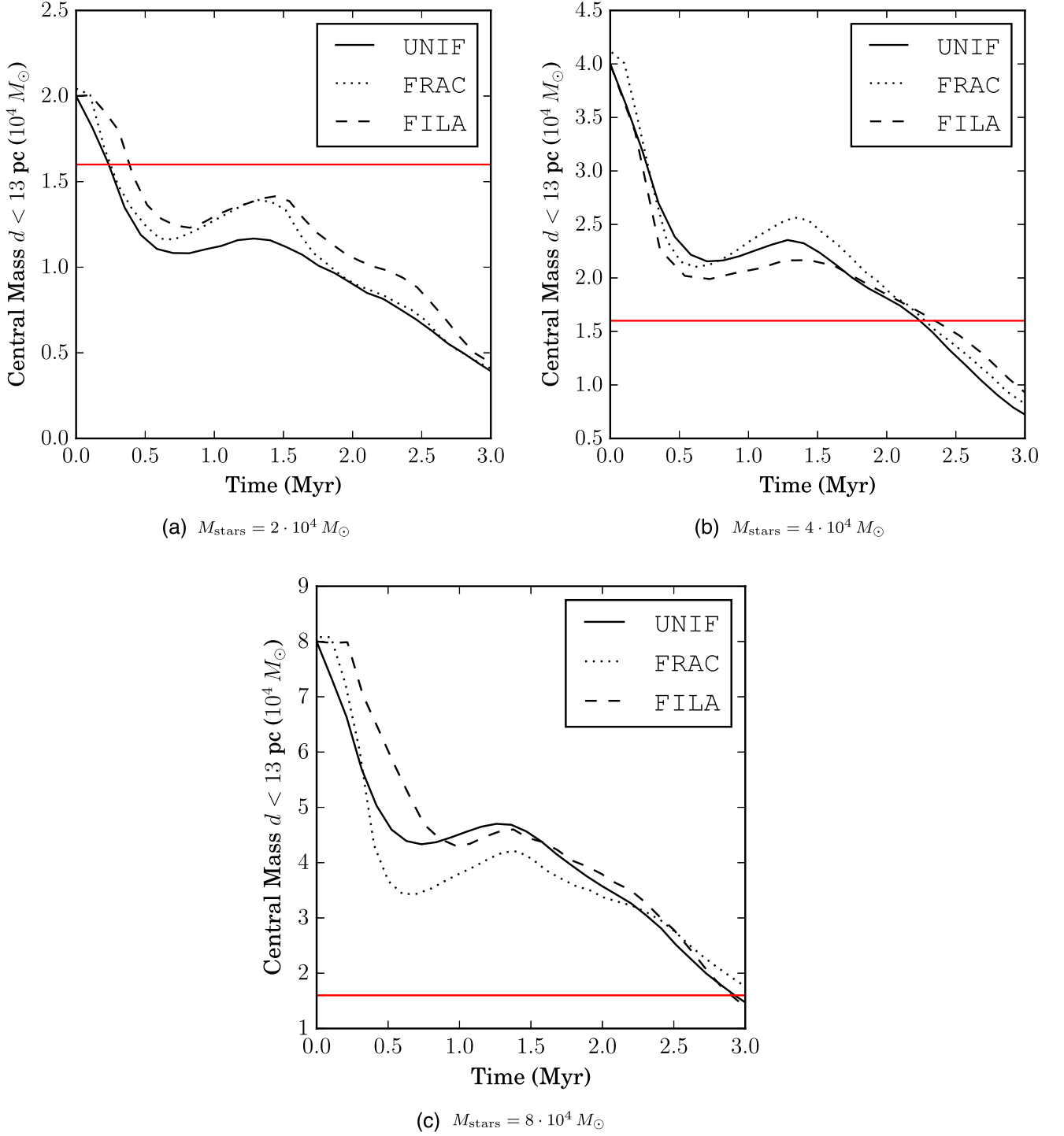
(a) $M_{stars} = 2 \cdot 10^4 \, M_\odot$

(b) $M_{stars} = 4 \cdot 10^4 \, M_\odot$

(c) $M_{stars} = 8 \cdot 10^4 \, M_\odot$

Figure 7. Evolution of the stellar mass within a projected distance of 13 pc from the centre of the cluster. We show the results for UNIF, FRAC, and FILA cluster models (solid, dotted, and dashed, respectively) over 3 Myr. All models have initial parameters $a_{gas} = 10$ pc, $a_{stars} = 7$ pc, $\tau_{delay} = 1.5$ Myr, $\tau_{exp} = 1.5$ Myr and varying stellar mass. The horizontal red line indicates the observed central mass $\sim 1.6 \times 10^4 \, M_\odot$ (Wright et al. 2015). We find that an initial mass of $\sim 8 \times 10^4 \, M_\odot$ reproduces the observed central density.

Table 1. Parameters of the 'best-fitting' model, used to reproduce the properties of the observed stellar population of Cyg OB2.

Type	M_{stars} (M$_\odot$)	a_{stars} (pc)	γ	P_0	D_0	$M_{gas,\,0}$ (M$_\odot$)	a_{gas} (pc)	τ_{delay} (Myr)	τ_{exp} (Myr)
FILA	8×10^4	7	5.8	1	2.5	7.9×10^6	10	1	1.5
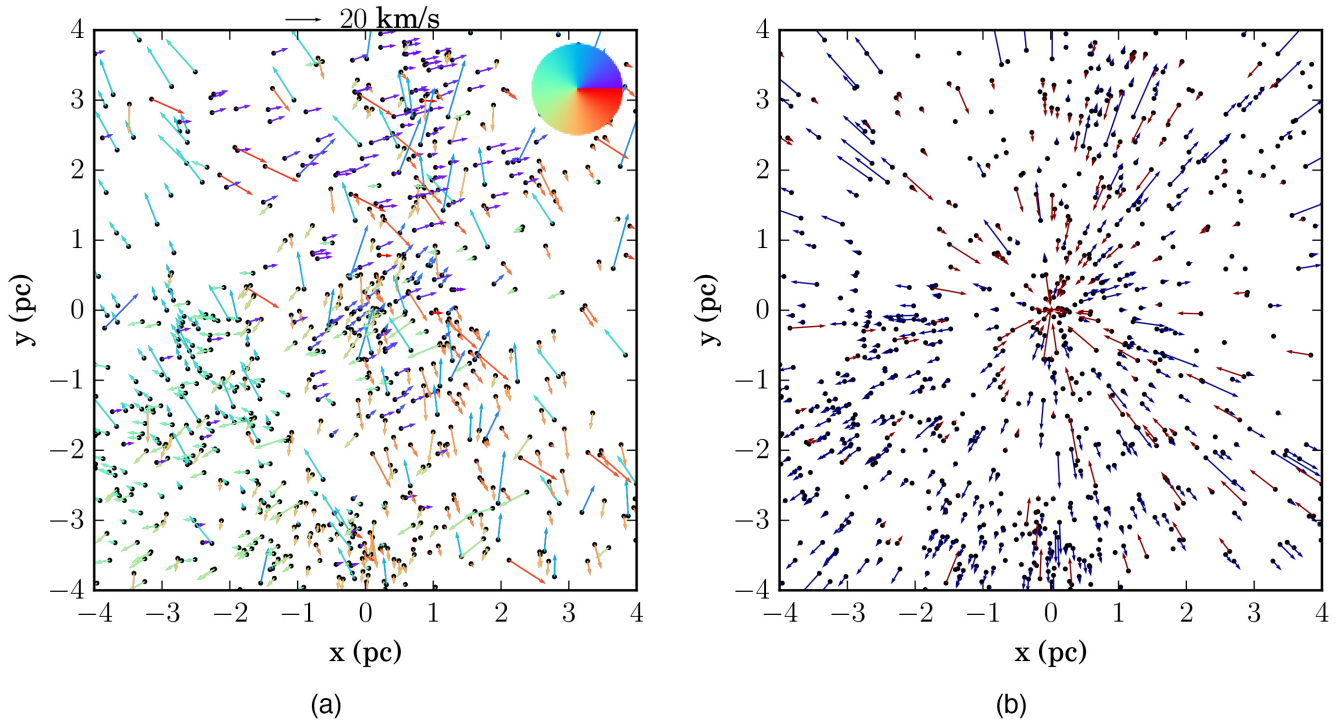
Figure 8. Velocity field of a subset of 800 stars in the central region of our chosen model (summarized by the parameters in Table 1) after 3 Myr of evolution. In Fig. 8(a) velocity vectors are colour coded by their direction to illustrate the underlying substructure; a correlation can be seen between position and velocity vectors. In Fig. 8(b) only the radial components in the plane of the sky are shown, coloured blue for stars moving outwards from the centre and red for infalling stars. There is no clear bias between infalling and outgoing velocities – see the text for details. Similarly, Wright et al. (2016) found correlations between position and velocity vectors, and that Cyg OB2 shows no sign of expansion from the apparent centre.
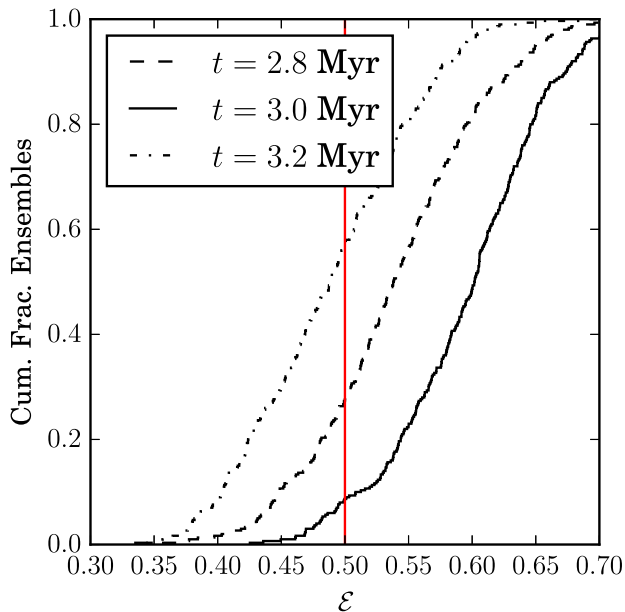
Figure 9. The cumulative fraction of the number of ensembles [each defined to be a subset of 800 stars in the Wright et al. (2016) field of view] with expansion parameter $\mathcal{E}$ (equation 10) in our chosen model. A value of $\mathcal{E} \approx 0.5$, which was found by Wright et al. (2016) for Cyg OB2, would observationally be taken as an indication that no expansion is occuring.

values for our model, we conclude that $\mathcal{E}$ alone is not a sufficient metric to draw conclusions on the expansion of a substructured association. For further discussion on the kinematic indicators of expansion in OB associations, see Baumgardt & Kroupa (2007) and Ward & Kruijssen (2018).

In the remainder of this work we will first revisit the disc population in our model, checking that the population is consistent with the known disc fractions in the region. Subsequently we will explore predictions for the disc mass and radius distribution relevant for future observations in the region.

4.4 Disc properties

In what follows we will consider a FILA model with the properties described in Table 1. We fix the α-viscosity of the disc population with the derived value $\alpha = 10^{-2}$ (Section 4.2). As in Section 4.2 all discs are assumed to have an initial mass that is uniformly distributed between 1 and 10 per cent of their host star mass (see Section 3.2.2), and scale radius as in equation (8). We consider the same range of stellar masses 0.5–2 $M_\odot$ and calculate the evolution of a subset of 5000 discs.

4.4.1 Disc fractions in best-fitting model

The disc fraction distribution in our best-fitting model after ∼3 Myr is summarized by Fig. 10, in which we show the surviving disc fraction as a function of projected FUV flux (Fig. 10a) with the spatial distribution and projected F_{FUV} in Fig. 10(b). We find that after 3 Myr the number of surviving discs is slightly overestimated
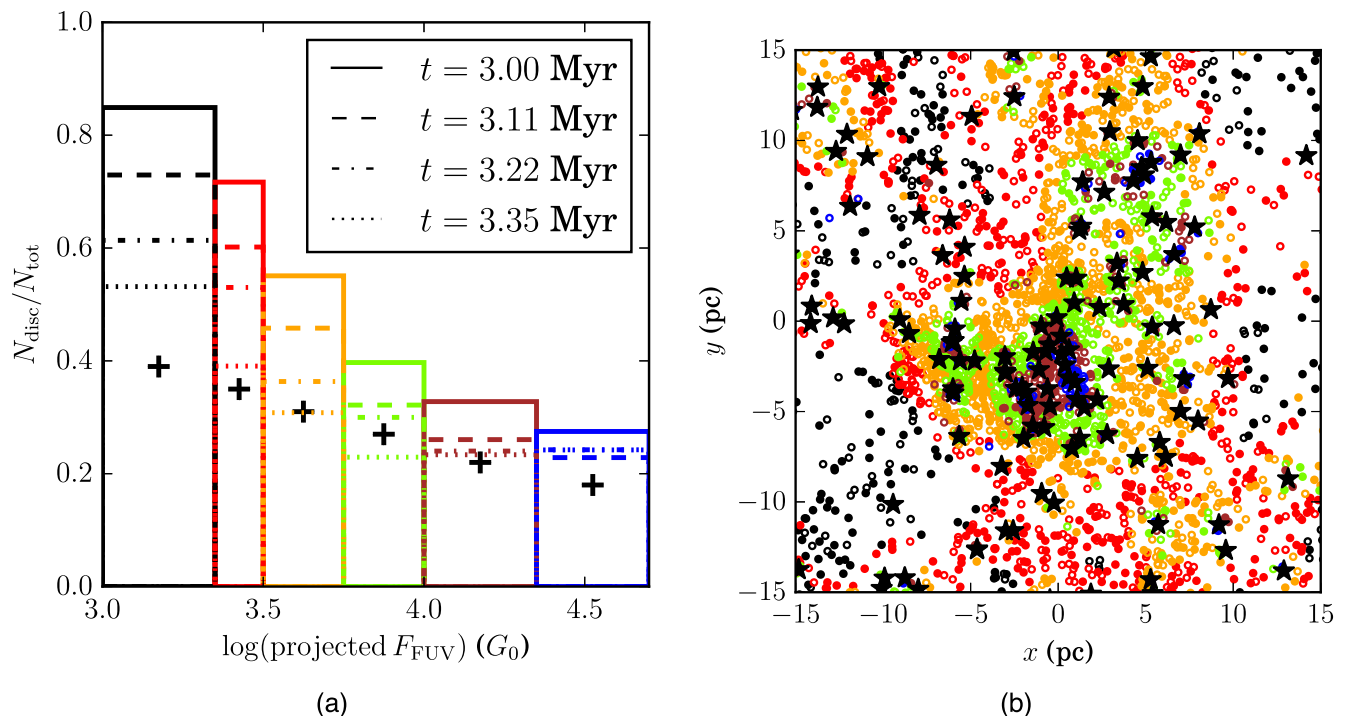
Figure 10. Model of the disc population in a model described by the parameters in Table 1. In Fig. 10(a) we show the disc fraction as a function of FUV flux, calculated by projected distance to massive stars, at varying times. These fractions are in good agreement with the observed disc fractions, indicated by the black crosses. In Fig. 10(b) we show the physical distribution of the disc population after 3 Myr, colour coded by the projected FUV flux as in Fig. 10(a). The star markers represent the positions of stars with a mass $> 10\,M_\odot$. The open circles represent a disc with a mass $< 10^{-5}\,M_\odot$, while the filled circles are 'surviving' discs with a greater mass (c.f. fig. 3 in Guarcello et al. 2016).

in our model, particularly at the lower FUV fluxes. There are two reasons why we expect this to be the case. First, extinction in the FUV may decrease before gas is fully removed from the cluster. If gas is expelled due to the flux from massive stars, then the central, highly irradiated environments would become less dense and allow efficient photoevaporation at earlier times. Additionally, clumpy gas distributions may have a similar effect in reducing extinction during this period. Secondly, internal photoevaporation due to the stellar host depletes the gas content even when a PPD evolves in isolation. This speeds up destruction time-scales, particularly in regions of lower F_{FUV}, where the mass-loss rates induced by internal and external photoevaporation become comparable.

The influence of the above considerations is uncertain and we therefore do not attempt to model them here. Our model does however reproduce the correct disc fractions within a reasonable period of time, particularly at $F_{FUV} \gtrsim 3000\,G_0$. We conclude that the observations of Guarcello et al. (2016) can be explained by external photoevaporation of the PPD population in Cyg OB2.

4.4.2 Disc mass and FUV flux environment

To make predictions about the disc population in Cyg OB2 for comparison with future observations we consider PPD mass as a function of FUV flux (Fig. 11). We find that, if used in isolation, the local flux experienced by a given star is a poor predictor of the disc mass. Correlation with real or projected FUV flux only becomes clear when the host mass, to which the final PPD mass is closely correlated (as demonstrated by the colour gradient in Fig. 11 and discussed in Section 4.4.3), is also taken into account. In particular,

we expect that low-mass stars ($< 1\,M_\odot$) in the centre of Cyg OB2 host exclusively low-mass discs ($\lesssim 10^{-3}\,M_\odot$, if any).

Without taking into account stellar mass, can we find differences in disc properties between PPDs in apparently high versus low FUV flux environments? To answer this, we must consider the sensitivity limit for future observations. Considering *ALMA* band 6 sensitivity, reasonable integration times ($\sim$30 min) for a survey sample suggest flux densities down to $F_\nu(850\,\mu m) \sim 40\,\mu Jy$ can be detected. At the distance of Cyg OB2 this means that dust masses can be established down to a few $M_\oplus$ (Andrews & Williams 2005). The corresponding total disc masses are $M_{disc} \sim 10^{-3}\,M_\odot$ if the gas to dust ratio is $\Sigma_{gas}/\Sigma_{dust} = 10^2$. Given that the PPDs are likely to be gas depleted by external photoevaporation, the latter assumption is probably not accurate for many discs (Ansdell et al. 2016), and this complicates the interpretation of observations. None the less, we show the cumulative PPD mass fraction after 3 Myr for two FUV flux bins in Fig. 12. While disc masses are indeed suppressed at higher projected FUV flux, considering the sensitivity limit of *ALMA* makes finding differences between the two populations impractical. A sample of several 100s of PPDs would be required to find a difference between the total population in high- and low FUV flux environments (including non-detections). We find that similar sample sizes would be required to find differences in disc outer radius distributions in the two environments.

4.4.3 Stellar mass independent disc initial conditions

In obtaining the results in Section 4.4.2 we have already assumed that the initial disc mass is dependent on the stellar mass of the host.
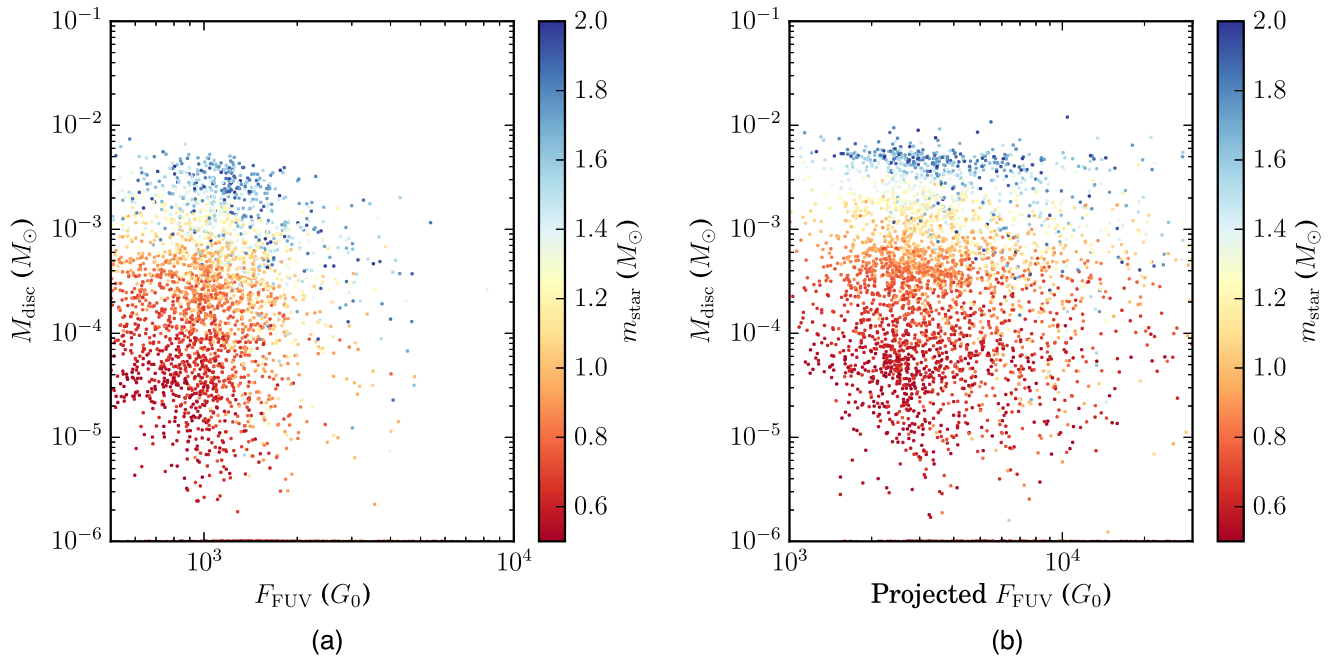
Figure 11. PPD mass after 3 Myr in our chosen model (described by the parameters in Table 1) as a function of real and projected FUV flux (Figs 11a and b, respectively). Points are colour coded by the mass of the host star. Initial disc masses are drawn from a uniform distribution between 1 per cent and 10 per cent of the host mass. In the context of Fig. 10, discs with masses $< 10^{-5}$ M$_\odot$ are considered 'destroyed'. We find that F_{FUV} is a poor indicator of disc mass.
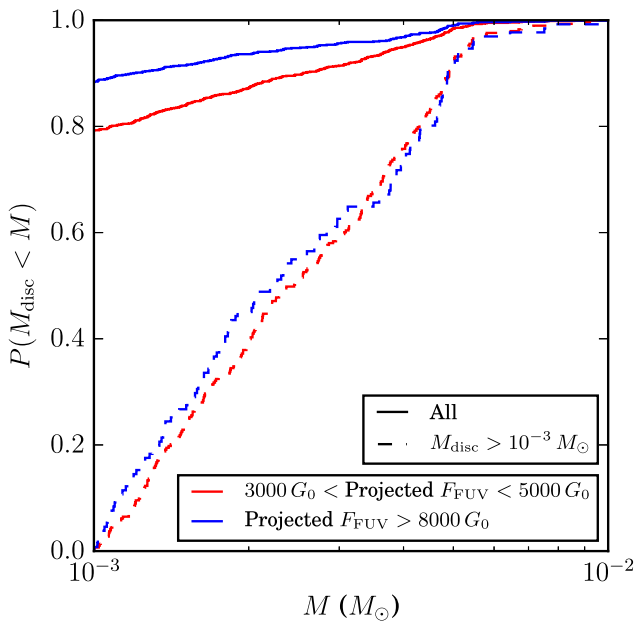
Figure 12. Cumulative fraction of disc mass after 3 Myr in our chosen model. The solid lines are for the entire disc population, while the dashed lines include only discs which have $M_{\mathrm{disc}} > 10^{-3}$ M$_\odot$. The disc population is divided up by projected (observed) FUV flux; the red lines are for stars experiencing an apparent F_{FUV} in the range 3–5 $\times$ 10^3 G$_0$, while the blue lines correspond to stars with $F_{\mathrm{FUV}} > 8 \times 10^3$. A large sample of all discs would be required to detect differences between the masses in the two FUV flux bins.

We wish to confirm our results are not sensitive to this assumption. We therefore recalculate the PPD evolution in our model under the assumption that the initial disc mass is uncorrelated to the stellar mass. To this end we draw the initial disc masses from a lognormal distribution:

$$M_{\mathrm{disc},0}/\mathrm{M}_\odot = e^{\mu + \sigma X}$$

where the random variable $X \sim \mathcal{N}(0, 1)$ is drawn from a standard normal distribution, uncorrelated with m_{star}. The values of $\mu = -3.25$ and $\sigma = 0.7$ are chosen such that the mean and dispersion of $M_{\mathrm{disc}, 0}$ match those chosen for the stellar mass dependent initial conditions. The scale radius R_1 is again defined according to equation (8). This distribution of initial conditions recovers similar disc fractions as a function of projected F_{FUV} (Fig. 13). The resulting disc mass distribution is shown in Fig. 14. Our findings do not differ greatly from those in Fig. 11, except for a predictable weaker correlation between final disc mass and host mass.

4.4.4 Disc mass dependence on host mass

The relationship between final disc mass and stellar mass is considered in Fig. 15(a) (Fig. 15b) for disc masses initially correlated (uncorrelated) with the host star mass. We obtain power-law indices ($M_{\mathrm{disc}} \propto m_{\mathrm{star}}^{\beta}$) $\beta = 3.93 \pm 0.11$ and 2.75 ± 0.12, respectively. In both cases this is a substantially more superlinear relationship than in local PPD populations that have not been significantly photoevaporated ($1 < \beta < 1.9$ Andrews et al. 2013; Pascucci et al. 2016). Physically this is because $\dot{M}_{\mathrm{wind}}$ is strongly dependent on stellar mass such that discs around low-mass stars are depleted much faster (due to a shallower potential) than those around high-mass stars for a fixed flux and disc radius (Haworth et al. 2018b). In regions where a disc population has undergone
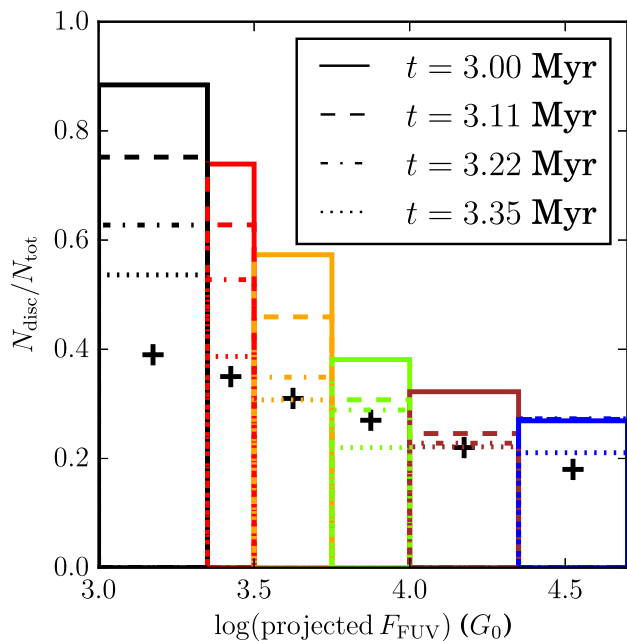
Figure 13. As in Fig. 10(a) but for a distribution of initial disc masses independent of the stellar host mass (see the text for details). This demonstrates that reproducing the observed disc fractions is not sensitive to the choice of PPD initial conditions.
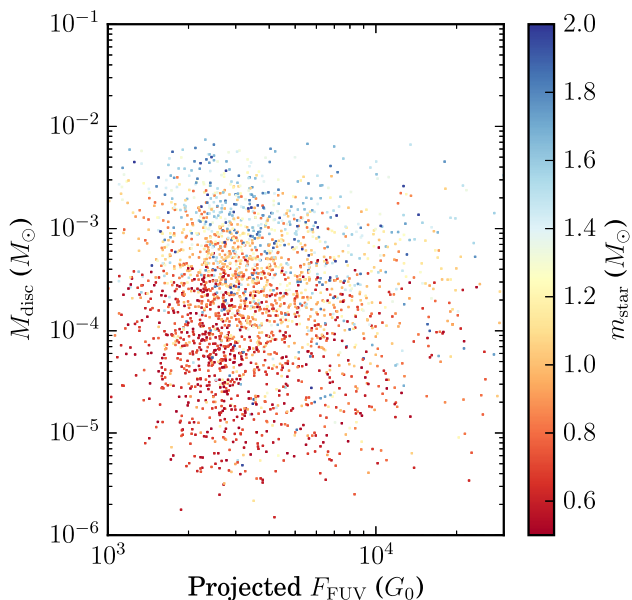

Figure 14. As in Fig. 11(b) but for a distribution of initial disc masses independent of the stellar host mass (see the text for details).

significant photoevaporation we then expect lower mass stars to host lower mass PPDs. Even if it proves impossible to obtain sufficiently large samples of mm-based mass determinations in Cyg OB2 in order to conduct the comparison made in Fig. 12, an alternative way to test the role of external photoevaporation would be to examine any evidence for steep disc mass–stellar mass relationship.

To estimate whether detecting large β values is possible in Cyg OB2, we extract a subset of 20 discs from our model, choosing them such that they lie in a region of projected FUV flux $3000\,G_0 < F_{FUV} < 8000\,G_0$. A lower limit of $3000\,G_0$ is appropriate since below this Figs 10(a) and 13 suggest that alternative processes to external photoevaporation have a comparable influence on disc evolution. We also select stellar masses to be approximately uniformly distributed between 0.5 and $2\,M_\odot$. We assume error of 30 per cent in M_{disc}, with $M_{disc} < 10^{-3}\,M_\odot$ constituting a non-detection, and a 10 per cent error in M_{star}. We then attempt to fit a power law using the LINMIX package (Kelly 2007) for a number of different PPD subsets. An illustrative example of such an exploration is shown in Fig. 16. In all cases we find that the fit effectively discounts power-law relations with $\beta \leq 1.9$. Values of $\beta \leq 1.9$ are similarly discounted in the model with stellar host mass independent disc initial conditions. Our findings suggest that, if a sample is carefully selected, evidence of external photoevaporation should be detectable in future observations of Cyg OB2. Indeed, Ansdell et al. (2017) find a steepening with age in this relationship across different regions that could be due to photoevaporation. To the contrary, Eisner (2018) find a shallower disc mass–host mass relationship in the strongly irradiated discs of the Orion Nebula Cluster; this could be the result of the youth or complex star formation history of the stellar population (Beccari et al. 2017; Kroupa et al. 2018). Disentangling these effects requires a detailed modelling of those regions, such as that presented in this paper.

One might ask whether it is possible to find signatures of underlying substructure within a population of PPDs. Given that the dynamical history is linked to the irradiation by FUV photons, it may be possible to detect distinct groups in the mass distribution of a disc sample. As discussed previously, in an externally photoevaporated population, disc properties are more strongly correlated with host mass than FUV flux. Therefore considering disc properties as a function of host mass is the best chance of finding distinct groups within a sample. This possibility is explored in Fig. 15, where the largest scale fractal membership is indicated for each PPD. We find that the mass distribution does not demonstrate a clear segregation between groups. The subgroups are in themselves massive ($\sim 10^4\,M_\odot$) and the high-mass end of the IMF is therefore well sampled in each filament. It is possible that for smaller scale substructure (with filaments of mass $< 10^3\,M_\odot$, see Winter et al. 2018b) a less well-sampled IMF might mean that different filaments have quite different local F_{FUV}. In this case we should expect to see a distinct PPD mass and outer radius distributions between filaments.

4.4.5 Disc radii

An alternative observable property, the outer disc radius R_{out}, may prove to be a better probe of substructure in future observations. This is because, while M_{disc} is depleted over the entire lifetime of the disc, the outer radius in regions of strong FUV flux is set by a balance between photoevaporative mass-loss and viscous expansion on short time-scales. We have so far neglected discussion of disc radius simply because resolving disc radii down to ~ 10 s au is challenging in a region such as Cyg OB2; the highest resolution of *ALMA* is ~ 0.02 arcsec, corresponding to ~ 30 au at 1.33 kpc distance. However, because it may be possible to resolve disc radii to sufficient accuracies in closer young stellar environments, we illustrate the distribution of disc radii in Fig. 17. There are some
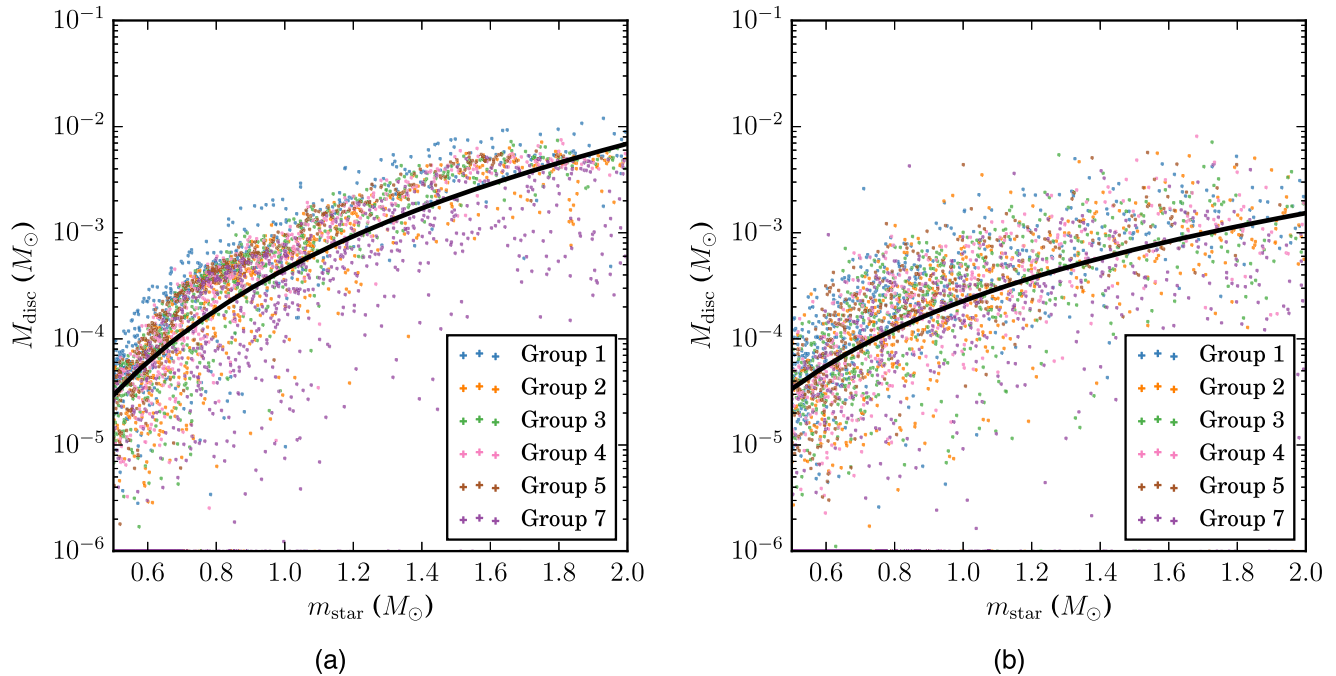
Figure 15. PPD mass distribution after 3 Myr of evolution in our chosen model (see the text and Table 1 for details). In Figs 15(a) and (b) initial disc masses are dependent on and independent of stellar host mass, respectively. The black line follows $(M_{disc}/M_\odot) = 4.5 \times 10^{-4} (m_{star}/M_\odot)^{3.9}$ in Fig. 15(a), and $(M_{disc}/M_\odot) = 2.3 \times 10^{-4} (m_{star}/M_\odot)^{2.8}$ in Fig. 15(b). The points are colour coded by the largest scale fractal sub-group to which they belong.
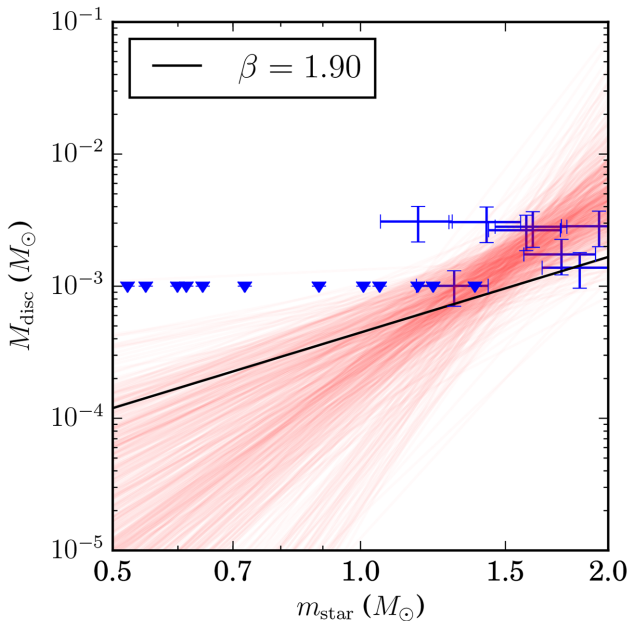
Figure 16. A subset of 20 discs of those shown in Fig. 15(a) (after 3 Myr of evolution), chosen to be approximately uniformly distributed over a range of stellar masses 0.5–2 $M_\odot$. All discs are also selected such that they are in an environment where the projected flux has an instaneous value $3000\,G_0 < F_{FUV} < 8000\,G_0$. Discs with $M_{disc} < 10^{-3}\,M_\odot$ are considered upper limits (non-detections). The red lines are a subset of samples from the posterior distribution obtained from Markov chain Monte Carlo modelling (using the LINMIX package – Kelly 2007). The black line is a model with $\beta = 1.9$ selected from the posterior distribution such that the true β is greater than this value with 2σ confidence.

indications of different radius distributions between different fractal associations, but no clear segregation between them. The majority of discs have $R_{disc} < 60$ au which would require <0.05 arcsec resolution at the distance of Cyg OB2. We note that outer disc radius measurements can be subject to large uncertainties, and that the dust emission is frequently less extended than the gas (e.g. Birnstiel et al. 2010; Guilloteau et al. 2011; de Gregorio-Monsalvo et al. 2013). This discrepancy may be less problematic in regions where disc radii are externally suppressed (for example close stellar encounters may result in wavelength-independent PPD outer radius measurements, as in the case of the disc around HV Tau C – Monin & Bouvier 2000; Winter et al. 2018c). This assumption requires further study into gas-dust physics in externally photoevaporating discs [see Cleeves et al. (2016) for discussion of gas and dust evolution in an FUV-irradiated PPD]. Overall we see the same trend as in disc masses that the outer radius is correlated with host mass. This is again because $\dot{M}_{wind}$ decreases with m_{star}, such that the radius at which viscous expansion is in equilibrium with FUV-induced mass-loss is more extended for more massive host stars.

5 CONCLUSIONS

Using *N*-body simulations and viscous disc evolution models we have successfully reproduced the properties of Cygnus OB2, including the stellar kinematics and the surviving PPD fractions as a function of projected FUV flux. Our modelling supports the following scenario:

(i) If the viscous evolution of PPDs is well described by a Shakura & Sunyaev α-parameter $\alpha = 10^{-2}$ ($\tau_{visc} \approx 0.5$ Myr for a solar mass star), then expulsion of the primordial gas content in the
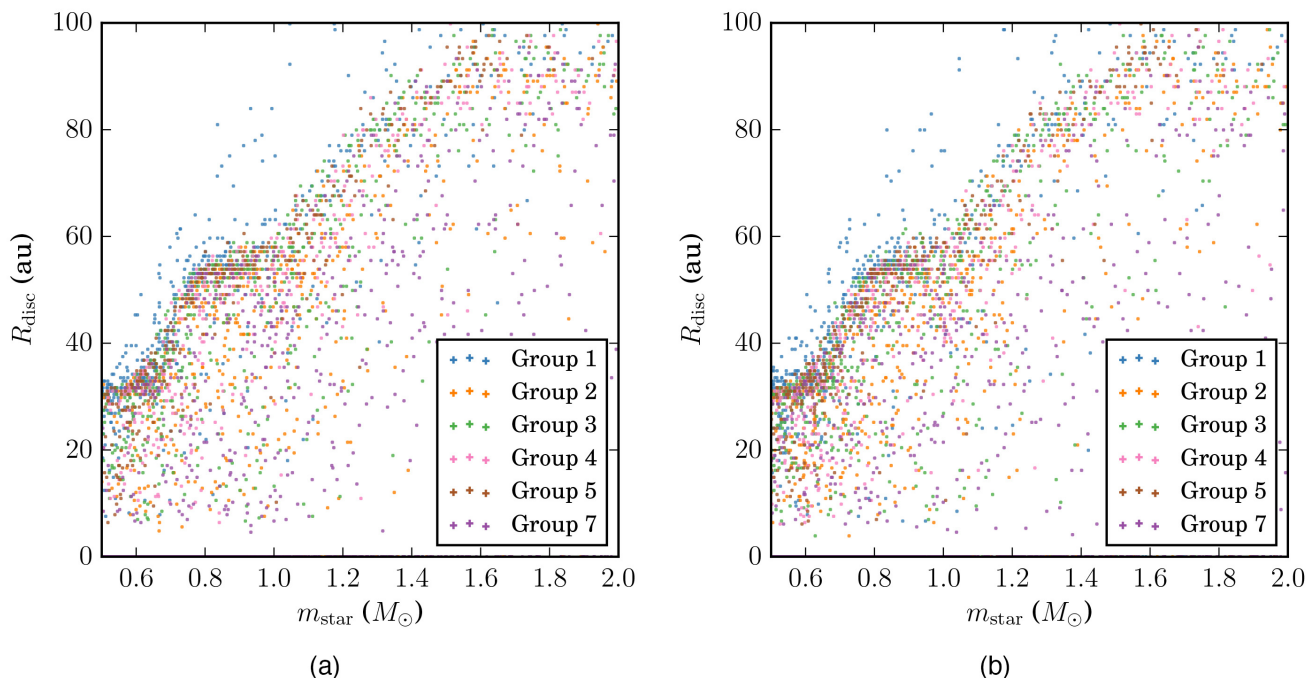
Figure 17. As in Fig. 15 but for disc outer radius distributions. In Fig. 17(a) initial disc masses are drawn from a distribution which scales linearly with stellar host mass, while in Fig. 17(b) the initial PPD mass is not correlated to host mass. The points are coloured by the largest scale fractal membership. We find that the outer radii are largely independent of disc initial conditions and are correlated with stellar host mass.

region must have concluded ∼0.5 Myr ago. Approximately 0.5 Myr of exposure to strong FUV fields is required to reproduce the current disc survival rates as a function of (projected) flux. This value of α will be an upper limit if FUV extinction due to the primordial gas was not efficient (because of a clumpy spatial distribution, for example).

(ii) The initial three-dimensional velocity dispersion must have been ∼50 km s^{-1} in order to be consistent with the present-day central velocity dispersion. This is large with respect to observed stellar populations, even for OB associations (e.g. Ward & Kruijssen 2018 and references therein). However, velocity gradients ∼10 km s^{-1} pc^{-1} are found across GMCs, particularly in the case of cloud–cloud collision (Wu et al. 2015; Bisbas et al. 2018; Pols et al. 2018).

(iii) Anisotropy in the present-day velocity dispersion requires the presence of primordial subtructure. We find that Cyg OB2 must have been comprised of large-scale filaments (or fractal clumps), with a mass ∼10^4 M$_\odot$.

(iv) In such a model, a gas content of ∼8×10^6 M$_\odot$ is required to maintain initial virial equilibrium. This is massive compared to the known distribution of molecular cloud masses in the Milky Way (Longmore et al. 2014).

(v) The total stellar mass required to sustain a sufficient central mass after 3 Myr is ∼8×10^4 M$_\odot$. This suggests a star formation efficiency of ∼1 per cent.

(vi) The apparent lack of expansion measured by Wright et al. (2016) need not be interpreted as evidence of no physical expansion of the stellar population. We find that our (expanding) model is equally consistent with an expansion parameter $\mathcal{E} \approx 0.5$. Such a measurement can only be interpreted probabilistically for an association with large-scale substructure.

The primary caveat of these conclusions is that the gas expulsion time-scale derived by disc fractions is degenerate with α. Our choice ($\alpha = 10^{-2}$, although this is in turn dependent on choice of scale radius R_1 – see equation 9) yields a good fit to the disc fractions and also allows us to reproduce kinematic observations with gas expulsion time-scale $\tau_{gas} = 2.5$ Myr. In future, observations of PPD populations in regions with a strong FUV flux but with more modest velocity dispersions (and primordial gas density) might offer further constraints for α.

Finally we make predictions for future observations of the disc mass and radius distribution in Cyg OB2. We find that samples of PPDs in highly FUV-irradiated environment have significantly reduced masses and outer radii than in regions of more modest flux. However, taking into account sensitivity limits, statistically observing these differences requires sample sizes of $\gtrsim$ 100s of discs in both high- and low FUV flux bins. This is similarly true for disc outer radii, and makes probing the difference between disc property distributions as a function of FUV environment directly impractical at present.

In Cygnus OB2 we expect a strong correlation between stellar mass and disc mass ($M_{disc} \propto m_{star}^\beta$, with $\beta > 2$) which is a consequence of the fact that, for a disc with given radius and in a given FUV environment, the mass-loss rate is higher in the shallower potential of low-mass stars. This effect should be clear in a sufficiently large sample of irradiated discs in any environment. In Cygnus OB2, we demonstrate that – taking into account the finite sensitivity of *ALMA* – it would be sufficient to target around 20 stars of known mass in order to demonstrate a value of β that is steeper than the canonical value ∼1–1.9 which is seen in non-irradiated disc samples. We conclude that, pending empirical confirmation, discs around low-mass stars born in environments of

strong FUV flux are likely to have a significantly depleted mass budget for planet formation. Indeed, unless dust within PPDs can rapidly grow to size scales where it is immune to photoevaporative stripping (e.g. Youdin & Goodman 2005), planet formation may be completely supressed for such host stars (Haworth et al. 2018a).

REFERENCES

Aarseth S. J., 2003, Gravitational N-Body Simulations, Cambridge University Press, Cambridge

Adams F. C., 2010, ARA&A, 48, 47

Ali A., Harries T. J., Douglas T. A., 2018, MNRAS, 477, 5422

Anderson K. R., Adams F. C., Calvet N., 2013, ApJ, 774, 9

André P., Di Francesco J., Ward-Thompson D., Inutsuka S.-I., Pudritz R. E., Pineda J. E., 2014, Protostars and Planets VI, University of Arizona Press, Arizona, p. 27

Andrews S. M., Williams J. P., 2005, ApJ, 631, 1134

Andrews S. M., Rosenfeld K. A., Kraus A. L., Wilner D. J., 2013, ApJ, 771, 129

Ansdell M. et al., 2016, ApJ, 828, 46

Ansdell M., Williams J. P., Manara C. F., Miotello A., Facchini S., van der Marel N., Testi L., van Dischoeck E. F., 2017, AJ, 153, 240

Armitage P. J., 2000, A&A, 362, 968

Baraffe I., Chabrier G., Gallardo J., 2009, ApJ, 702, L27

Bate M. R., 2018, MNRAS, 475, 5618

Baumgardt H., Kroupa P., 2007, MNRAS, 380, 1589

Bica E., Bonatto C., Dutra C. M., 2003, A&A, 405, 991

Beccari G. et al., 2017, A&A, 604, 22

Birnstiel T. et al., 2010, A&A, 516, L14

Bisbas T. G. et al., 2018, MNRAS, 478, L54

Bonnell I. A., Davies M. B., 1998, MNRAS, 295, 691

Bonnell I. A., Clark P., Bate M. R., 2008, MNRAS, 389, 1556

Breslau A., Steinhausen M., Vincke K., Pfalzner S., 2014, A&A, 565, A130

Butt Y. et al., 2003, ApJ, 597, 494

Castelli F., Kurucz R. L., 2004, preprint (arXiv:e-print)

Clarke C. J., 2007, MNRAS, 376, 1350

Clarke C. J., Pringle J. E., 1993, MNRAS, 261, 190

Cleeves L. I., Öberg K. I., Wilner D. J., Huang J., Loomis R. A., Andrews S. M., Czekala I., 2016, ApJ, 832, 110

Comerón F., Pasquali A., 2012, A&A, 543, A101

Concha-Ramírez F., Vaher E., Portegies Zwart S., 2019, MNRAS, 482, 732

Craig J., Krumholz M. R., 2013, ApJ, 769, 150

Cuello N. et al., 2018, MNRAS, 483, 4114

Dale J. E., Bonnell I., 2011, MNRAS, 414, 321

Dale J. E., Ngoumou J., Ercolano B., Bonnell I. A., 2014, MNRAS, 442, 694

de Gregorio-Monsalvo I. et al., 2013, A&A, 557, A133

Drew J. E., Greimel R., Irwin M. J., Sale S. E., 2008, MNRAS, 386, 1761

Eisner J. A. et al., 2018, ApJ, 860, 77

Elson R. A. W., Fall S. M., Freeman K. C., 1987, ApJ, 323, 54

Facchini S., Clarke C. J., Bisbas T. G., 2016, MNRAS, 457, 3593

Fatuzzo M., Adams F. C., 2008, ApJ, 675, 1361

Goodwin S. P., 2009, Ap&SS, 324, 259

Goodwin S. P., Whitworth A. P., 2004, A&A, 413, 929

Guarcello M. G. et al., 2013, ApJ, 773, 135

Guarcello M. G. et al., 2016, preprint (arXiv:1605.01773)

Guarcello M. G., Prisinzano L., Micela G., Damiani F., Peres G., Sciortino S., 2007, A&A, 462, 245

Guarcello M. G., Wright N. J., Drake J. J., García-Alvarez D., Drew J. E., Aldcroft T., Kashyap V. L., 2012, ApJS, 202, 19

Guilloteau S., Dutrey A., Piétu V., Boehler Y., 2011, A&A, 529, A105

Habing H. J., 1968, Bull. Astron. Inst. Neth., 19, 421

Haisch K. E., Jr., Lada E. A., Lada C. J., 2001, ApJ, 553, L153

Hanson M. M., 2003, ApJ, 597, 957

Hartmann L., Calvet N., Gullbring E., D'Alessio P., 1998, ApJ, 495, 385

Haworth T. J., Facchini S., Clarke C. J., Cleeves L. I., 2017, MNRAS, 468, L108

Haworth T. J., Facchini S., Clarke C. J., Mohanty S., 2018a, MNRAS

Haworth T. J., Clarke C. J., Rahman W., Winter A. J., Facchini S., 2018b, 481, 452

Herbst W., Herbst D. K., Grossman E. J., Weinstein D., 1994, AJ, 108, 1906

Johnstone R. M., Fabian A. C., Taylor G. B., 1998, MNRAS, 298, 854

Kelly B. C., 2007, ApJ, 665, 1489

Kiminki D. C. et al., 2007, ApJ, 664, 1102

Kiminki D. C. et al., 2008, ApJ, 681, 735

Kiminki D. C., Kobulnicky H. A., Vargas Álvarez C. A., Alexander M. J., Lundquist M. J., 2015, ApJ, 811, 85

Kim J. S., Clarke C. J., Fang M., Facchini S., 2016, ApJ, 826, L15

Knödlseder J., 2000, A&A, 360, 539

Kroupa P., 2001, MNRAS, 322, 231

Kroupa P., Jeřábková T., Dinnbier F., Beccari G., Yan Z., 2018, A&A, 612, 74

Kruijssen J. M. D., 2012, MNRAS, 426, 3008

Kuznetsova A., Hartmann L., Ballesteros-Paredes J., 2018, MNRAS, 473, 2372

Lada C. J., Lada E. A., 2003, ARA&A, 41, 57

Longmore S. N. et al., 2014, Protostars and Planets VI, University of Arizona Press, Arizona, p. 291

Massey P., Thompson A. B., 1991, AJ, 101, 1408

Massey P., Johnson K. E., Degioia-Eastwood K., 1995, ApJ, 454, 151

Molinari S. et al., 2010, A&A, 518, L100

Monin J.-L., Bouvier J., 2000, A&A, 356, L75

Moran P. A. P., 1950, Biometrika, 37, 17

Murray N., 2011, ApJ, 729, 133

O'dell C. R., Wen Z., 1994, ApJ, 436, 194

Offner S. S. R., Hansen C. E., Krumholz M. R., 2009, ApJ, 704, L124

Ostriker E. C., 1994, ApJ, 424, 292

Pascucci I. et al., 2016, ApJ, 831, 125

Pfalzner S., Kaczmarek T., 2013, A&A, 559, A38

Pfalzner S., Vogel P., Scharwächter J., Olczak C., 2005, A&A, 437, 967

Pols S., Schwörer A., Schilke P., Schmiedeke A., Sánchez-Monge, Á., Möller T., 2018, A&A, 614, A123

Preibisch T., Zinnecker H., 1999, AJ, 117, 2381

Ribas, Á., Bouy H., Merín B., 2015, A&A, 576, A52

Rosotti G. P., Clarke C. J., Manara C. F., Facchini S., 2017, MNRAS, 468, 1631

Salpeter E. E., 1955, ApJ, 121, 161

Scally A., Clarke C., 2001, MNRAS, 325, 449

Scally A., Clarke C., 2002, MNRAS, 334, 156

Schaller G., Schaerer D., Meynet G., Maeder A., 1992, A&AS, 96, 269

Schneider N., Bontemps S., Simon R., Jakob H., Motte F., Miller M., Kramer C., Stutzki J., 2006, A&A, 458, 855

Shakura N. I., Sunyaev R. A., 1973, A&A, 24, 337

Spurzem R., 1999, J. Comput. Appl. Math., 109, 407

Störzer H., Hollenbach D., 1999, ApJ, 515, 669

Tobin J. J., Hartmann L., Furesz G., Mateo M., Megeath S. T., 2009, ApJ, 697, 1103

Vincke K., Pfalzner S., 2018, ApJ, 868, 1

Wang L., Spurzem R., Aarseth S., Nitadori K., Berczik P., Kouwenhoven M. B. N., Naab T., 2015, MNRAS, 450, 4070

Ward J. L., Kruijssen J. M. D., 2018, MNRAS, 475, 5659

Williams J. P., Cieza L. A., 2011, ARA&A, 49, 67

Winter A. J., Clarke C. J., Rosotti G., Booth R. A., 2018a, MNRAS, 475, 2314

Winter A. J., Clarke C. J., Rosotti G., Ih J., Facchini S., Haworth T. J., 2018b, MNRAS, 478, 2700

Winter A. J., Booth R. A., Clarke C. J., 2018c, MNRAS, 479, 5522

Wright N. J., Drake J. J., Drew J. E., Vink J. S., 2010, ApJ, 713, 871

Wright N. J., Drake J. J., Guarcello M. G., Aldcroft T. L., Kashyap V. L., Damiani F., DePasquale J., Fruscione A., 2014a, preprint (arXiv: 1408.6579)

Wright N. J., Parker R. J., Goodwin S. P., Drake J. J., 2014b, MNRAS, 438, 639

Wright N. J., Drew J. E., Mohr-Smith M., 2015, MNRAS, 449, 741

Wright N. J., Bouy H., Drew J. E., Sarro L. M., Bertin E., Cuillandre J.-C., Barrado D., 2016, MNRAS, 460, 2593

Wu B., Van Loo S., Tan J. C., Bruderer S., 2015, ApJ, 811, 56

Youdin A. N., Goodman J., 2005, ApJ, 620, 459

This paper has been typeset from a TEX/LATEX file prepared by the author.